Middle Pleistocene fluid infiltration with 10–15 ka recurrence within the seismic cycle of the active Monte Morrone Fault System (central Apennines, Italy)

(Article begins on next page)

Middle Pleistocene fluid infiltration with 10-15 ka recurrence within the seismic cycle of the active Monte Morrone Fault System (central Apennines, Italy)

Gianluca Vignaroli[1,*], Federico Rossetti[2], Lorenzo Petracchini[3], Valentina Argante[2,4], Stefano M. Bernasconi[5], Mauro Brilli[3], Francesca Giustini[3], Tsai-Luen Yu[6], Chuan-Chou Shen[7,8], Michele Soligo[2]

1 Dipartimento di Scienze Biologiche, Geologiche e Ambientali - Università degli Studi di Bologna, Bologna, Italy (gianluca.vignaroli@unibo.it)

2 Dipartimento di Scienze - Università degli Studi di Roma Tre, Roma, Italy

3 Istituto di Geologia Ambientale e Geoingegneria - Consiglio Nazionale delle Ricerche, Roma, Italy

4 Leibniz Institute for Applied Geophysics, Stilleweg 2, 30655 Hannover, Germany

5 ETH Zürich, Geological Institute, 8092 Zürich, Switzerland

6 Marine Industry and Engineering Research Center, National Academy of Marine Research, Kaohsiung 80661, Taiwan, ROC

7 High-Precision Mass Spectrometry and Environment Change Laboratory (HISPEC), Department of Geosciences, National Taiwan University, Taipei 10617, Taiwan, ROC

8 Research Center for Future Earth, National Taiwan University, Taipei 10617, Taiwan, ROC

* Corresponding author:

Gianluca Vignaroli
Dipartimento di Scienze Biologiche, Geologiche e Ambientali
Università degli Studi di Bologna
Via Zamboni, 67 – 40126 Bologna (Italy)
gianluca.vignaroli@unibo.it

Abstract

This study integrates field, geochronological and geochemical data to constrain fluid circulation in the damage and core zone of the seismogenic Monte Morrone Fault System (MMFS), central Apennines (Italy). Faulting along the MMFS evolved from a diffuse deformation at the damage zone towards progressive localisation of a narrower fault core and, finally, to (re)activation of discrete slip surfaces at shallower crustal conditions. Multiple generations of carbonate mineralisations, including veins and slickfibers, occur along the main fault surfaces. Carbonate mineralisations are locally fractured and incorporated in the surrounding cataclasites, documenting repetitive structurally-controlled fluid infiltration during transient episodes of permeability creation and destruction. Stable carbon and oxygen isotopes of the carbonate mineralisations document a dominant meteoric water source probably mixed with deeper circulating waters having longer residence time. Clumped-isotope yield formation temperatures of vein and slickenfibers in the range between 23 and 40 °C. U-Th dating of carbonate mineralisations yield Middle Pleistocene ages (from 268 to 189 ka BP), with a 10-15-ka cyclicity that we link to the coseismic rejuvenation of the structural permeability in the fault zone. We propose that fault-related mineralisations recorded the interactions among tectonic deformation and climate during the Quaternary. Our study is the first documentation of fault-controlled recurrence intervals in fluid infiltration in a seismically active fault of central Apennines.

1. Introduction

In the upper seismogenic crust, the growth of major faults includes creation/destruction of secondary permeability involving deformation and fluid pressure fluctuations in response to a continuous stress accumulation throughout the entire seismic cycle (e.g., Sibson, 1992; 2014; Hickman et al., 1995; Miller et al., 2004; Smeraglia et al., 2016; Fig. 1). The relationship between creation/destruction of secondary permeability in fault rocks and pulses of fluid ingress are sensitive gauges of crustal deformation, with implication on location and recurrence intervals of earthquakes. During the coseismic rupture, cataclastic processes and fracturing rejuvenate the internal architecture of the fault in response to heterogeneous strain localisation during fault growth and propagation (Sibson, 1992; Tesei et al., 2013; Delle Piane et al., 2017 and references therein). Structural permeability increases depending on fracture persistency, interconnectivity, and geometry, allowing enhanced fluid ingress in fault rocks (e.g., Caine et al., 1996; Rowland and Sibson, 2004; Cox, 2010; Sibson, 2014; Williams et al., 2015). Fluids migrate through the secondary permeability in hydrostatic condition if fault permeability is maintained by cycles of coseismic failures (e.g., Sibson and Rowland, 2003). In the interseismic/postseismic stage, mineral precipitation from circulating fluids progressively seals the fault zone permeability (e.g., Cox, 2010). This mechanism of permeability destruction sets the ground for the subsequent suprahydrostatic pressure build up, which may enhance coseismic failure at seismogenic depths and activation/reactivation of slip surfaces at shallower depths (e.g., Cox et al., 2001; Sibson, 2014; Smeraglia et al., 2016). Consequently, cycles of permeability creation and destruction characterise the fault zone evolution during the different stages of a seismic cycle, and the study of fluid circulation is, therefore, key to reconstruct the space-time distribution and evolution of fault permeability (Caine et al., 1996; Sibson and Rowland, 2003). In particular, the geochemical properties of the fluids infiltrating along structurally controlled pathway (faults and fractures) provide constraints on the scale and types of fluid circulation. The absolute ages of different generations of sealing mineralisations provide the timing of the fault activation/reactivation episodes. Reconstructing fault/host rock fluid interactions contributes to refine the recurrence model of seismic failure during the geological history of major fault systems.

The seismotectonic framework of the central Apennines is controlled by distributed extensional faulting (e.g., Cello et al., 1997; Galli et al., 2008; Faure Walker et al., 2010; Iezzi et al., 2019). Fault activity is typified by a continuous interaction and feedback between fault (re)activation and fluid migration during the complete seismic cycle (e.g., Smith et al., 2011; Collettini et al., 2013; Doglioni et al., 2014; Smeraglia et al., 2016; 2018; Barberio et al., 2017). Presently, instrumental (ISIDe database; http://terremoti.ingv.it/en/iside), historical (Rovida et al.,

2020; https://emidius.mi.ingv.it/CPTI15-DBMI15/index_en.htm) and paleoseismological (e.g.,

Galli et al., 2008 and references therein) datasets can help reconstruct activity and recurrence

intervals of seismogenic faults through the entire Holocene. Very few studies, however, provide

geological and geochronological constraints on the long-term tectonic activity of seismically active

normal faults. In this view, the occurrence of distinctive fabrics and mineralisations in faults has

been used to identify the relative chronological sequence of Quaternary deformation events during

the interseismic and the coseismic stages (Smeraglia et al., 2018; Vignaroli et al., 2020a).

In this study, we describe the structural relationships between tectonic structures and fluid

infiltration within the Monte Morrone Fault System (MMFS), an outstanding example of active

extensional faulting in the central Apennines (Fig. 2a,b). The MMFS consists of NW-SE-striking

normal fault strands, cutting across Pleistocene-to-Holocene continental deposits (Miccadei et al.,

1998; Galadini and Galli, 2000; Gori et al., 2011). The trace of the MMFS corresponds to a

regional-scale seismic gap with respect to the 2009 Mw 6.1 L'Aquila and the 2016-2017 Mw 6.0-

6.5 Amatrice-Norcia earthquakes, the last destructive seismic sequences in central Italy (e.g.,

Chiarabba et al., 2009; Chiaraluce et al., 2017). We document multiple generations of syn-tectonic

carbonate mineralisations within the damage and core zone of the MMFS. We constrained the

meso- and micro-scale structural properties, the $\delta^{13}C$ and $\delta^{18}O$ and clumped isotope signature, and

the U-Th ages of these carbonate mineralisations to reconstruct the fault-fluid interplay and its

spatio-temporal evolution during the different stages of the seismic cycle. In particular, by dating

the fault-related mineralisations, we fixed the absolute ages of the MMFS activation episodes.

Finally, we propose a conceptual model of recurrence intervals of Middle Pleistocene fluid

infiltration and fault interaction during the seismic cycle of the MMFS. This study could set the

ground for establishing a seismic recurrence model on regional-scale faults within the seismically

active tectonic setting of the central Apennines.

2. Geological Setting

2.1. The central Apennines

The central Apennines (Fig. 2a,b) is a roughly NW-SE-trending orogenic segment originated

from the Cenozoic oceanic subduction and subsequent continental collision between the European

and the Adria plates (e.g., Dewey et al., 1989; Boccaletti et al., 1990; Faccenna et al., 2001;

Carminati et al., 2010). The resulting fold-and-thrust belt (Fig. 2b) deformed rocks belonging to

different paleogeographic domains, including (a) limestones and dolostones of Mesozoic platforms-to-basin environments, and (b) flysch sediments of Tortonian-to-Pliocene foredeep basins (e.g., Vezzani et al., 2010; Cosentino et al., 2010). Crustal shortening operated through the activation of west-dipping, regional-scale thrusts in a general eastward migration of compressive fronts toward the Adriatic foreland (e.g., Barchi et al., 1998; Patacca et al., 2008).

The present-day structural setting of the central Apennines results from the progressive uplift of the early stacked units followed by extensional tectonics since the Pliocene. This post-orogenic phase has started from the hinterland (Tyrrhenian) side of the belt and migrated towards the foreland, generating mainly NW-SE-striking normal faults and the formation of large intermountain basins filled by transitional-to-continental Plio-Quaternary deposits (e.g., Malinverno and Ryan, 1986; Dewey, 1988; Martini and Sagri, 1993; Faccenna et al., 1997; Cavinato and DeCelles, 1999; Cavinato et al., 2002; Cosentino et al., 2017). Crustal thinning generated a complex network of major extensional faults arranged in both en-echelon and collinear geometry (e.g., Ghisetti and Vezzani, 2002; Galadini and Messina, 2004; Roberts and Michetti, 2004; Pizzi et al., 2017; Galli et al., 2019; Fig. 2b). The major normal faults extend to a depth of 10–15 km, with dip $\geq 45°$. Intermountain basins, mostly filled by continental deposits, often develop at the hanging wall of the master faults, whereas Mesozoic carbonates are exposed at their footwall, indicating kilometre-scale down-section stratigraphic displacements (e.g., Boncio et al., 2004; Roberts and Michetti, 2004; Galli et al., 2008; Lanari et al., 2021). The estimated Holocene throw rate for the major normal faults ranges from 0.3 to ~2 mm/yr (Roberts and Michetti, 2004; Cowie et al., 2017).

NW-SE-striking normal faults control the intense seismicity in the axial part of the central Apennines, as testified by both the historical (Rovida et al., 2020) and the recent and destructive events (the 1997 Colfiorito event, Mw 6.0; the 2009 L'Aquila event, Mw 6.1; the 2016-2017 Amatrice-Norcia sequence, Mw up to 6.5; Fig. 2b). Seismicity remains confined in the uppermost 10-12 km crustal section (Amato et al., 1998; Chiaraluce et al., 2017). Studies on fault slip rates (Roberts and Michetti, 2004; Faure Walker et al., 2010), paleoseismology (Galli et al., 2008; Galli et al., 2018; 2019) and global-positioning system (D'Agostino et al., 2011) confirm that the major normal faults are the locus of active deformation localisation at short- and long-term scales (up to 10^4 years). For the active normal faults, a 1-2 ka recurrence time for Mw > 6.5 earthquakes has been estimated based on paleoseimological constraints (Galli et al., 2008). Recent U-series ages for syn-tectonic mineralisations constrained the long-term activity in potentially-seismogenic structures of the central Apennines in the ~350-108 ka time interval (Smeraglia et al., 2018; Vignaroli et al., 2020a).

153   The fluid-assisted deformation in the central Apennines has been documented in faulted

154   carbonate and siliciclastic units through the analysis of syn-tectonic mineralisations (e.g., Maiorani

155   et al., 1992; Conti et al., 2001; Ghisetti et al., 2001; Agosta et al., 2008; Smeraglia et al., 2016;

156   2018; Vignaroli et al., 2020a; Curzi et al., 2021; Coppola et al., 2021). Most syn-tectonic

157   mineralisations preserve the geochemical signature of cold-water circulation at shallow depths,

158   suggesting a dominant meteoric/groundwater fluid circulation. It is noteworthy, that earthquake-

159   related fluid circulation is characterised by the interplay between transient permeability at the fault

160   damage zones and mixing of fluids from different reservoirs, in part also of deeper origin

161   (Smeraglia et al., 2018).

162

163   ### 2.2. The Monte Morrone Fault System

164   The MMFS consists of NW-SE-striking fault segments with an along-strike cumulative

165   length of ~25 km (e.g., Miccadei et al., 2002; Gori et al., 2011; Fig. 2c). The MMFS runs sub-

166   parallel and cuts across the SW-dipping, back-limb of the NW-SE-trending Monte Morrone

167   anticline, developed at the hanging wall of E-verging thrust sheets (e.g., Vezzani et al., 2010).

168   Thrusting involved a Mesozoic-Cenozoic basinal succession of limestones and marls evolving to

169   platform carbonates. Seismic profiles suggest that the MMFS penetrates the crust to a depth of 10-

170   12 km, accommodating more than 2 km of cumulative movement during the Pleistocene-Holocene

171   (Patacca et al., 2008). Subsidence at the hanging wall of the MMFS provided the space for

172   sedimentation of several hundred metres of alluvial–fluvial–lacustrine sediments that fill the

173   intermountain Sulmona Basin (e.g., Miccadei et al., 1998; Giaccio et al., 2009; Fig. 2d). In the

174   Sulmona Basin, the eastward dip and the fan geometry of the strata attest for syn-tectonic deposition

175   during normal-sense movement of the MMFS (e.g., Miccadei et al., 1998; Gori et al., 2011). Based

176   on geomorphic expressions and geological correlations, the Holocene slip rate of the MMFS has

177   been estimated to be between 0.4 and 1.1 mm/yr (Roberts and Michetti, 2004; Gori et al., 2011).

178   The MMFS developed through propagation and interaction of two parallel west-dipping

179   fault strands: the western fault system (WFS) and the eastern fault system (EFS) (Galadini and

180   Messina, 2004; Boncio et al., 2012; Gori et al., 2014). The WFS runs through the Roccacasale

181   village and extends from the Popoli village in the NW to the Pacentro village in the SE (Fig. 2c).

182   This strand consists of a complex network of NW-SE-striking (SW-dipping) fault segments

183   arranged in collinear and, subordinate, right-stepping en-echelon geometry. The exposure of the

184   WFS fault scarps near Roccacasale reveals almost planar and striated surfaces (Boncio et al., 2012)

185   covering an up to half a metre-thick fault core developed through multiple events of fabric

186 formation and rejuvenation in response to cyclic stress accumulation and dissipation (Ferraro et al.,
187 2018; 2019; Coppola et al., 2021). Occurrence of different cemented fault rocks, from matrix-
188 supported to grain-supported (Ferraro et al., 2018), and multiple microcrystalline calcite cement in
189 cataclastic-to-ultracataclastic layers (Ferraro et al., 2019; Coppola et al., 2021) suggests a co-
190 seismic fabric reworking during fluid-assisted deformation.

191 No major (i.e. Mw > 4) historical earthquakes are associated with the MMFS (Rovida et al.,
192 2020). The seismic source of the catastrophic 1706 event that hit the Sulmona Basin is still debated
193 (Galli et al., 2015) and possibly located around the adjacent Majella ridge (Fig. 2b). However,
194 archaeoseismic and paleoseismic constraints set the elapsed time for the MMFS since the last event
195 at ~1850 yr ago, which is compatible with the average recurrence time of the Apennine
196 seismogenic faults (Galadini and Galli, 2001; Galli et al., 2015). Barberio et al. (2017) monitored
197 several springs located within the Sulmona Basin and associated their hydrochemical variation to
198 the mainshocks of the 2016-2017 Amatrice-Norcia sequence. This hydrogeological setting suggests
199 an active structural permeability in the Monte Morrone area, potentially sensitive to seismic inputs.

200

201

202 **3. Materials and Methods**

203 Through the study of fault strands exposed near the Roccacasale village, we focused on the
204 structural permeability of the WFS by characterising its brittle structural architecture and the
205 associated fault-related carbonate mineralisations (see structural stops in Fig. 2e). Field criteria for
206 fault rock classification (e.g., Sibson, 1977; Braathen et al., 2004) have been used to identify and
207 characterise the fault structural fabrics, whereas classic kinematic criteria have been used to
208 determine the sense of shear (e.g., Petit, 1987).

209 We collected hand samples of fault rocks and carbonate mineralisation (Table 1). Optical
210 and back-scattered electron (BSE) microscopy was performed on oriented thin sections to
211 characterise the overprinting relationships among different generations of structures and carbonate
212 mineralisations that took place during faulting. Cold cathodoluminescence (CL) imaging were
213 performed using a Cambridge Image Technology Limited luminoscope Leica DM2700P optical
214 microscope (model Mk5-2; operating system at 9.9 kV with a beam current of 256 µA) at the
215 Department of Chemistry, Life Sciences, and Environmental Sustainability of the University of
216 Parma.

217   U-Th dating was carried out on (1) a Thermo Electron Neptune multi-collector inductively

218 coupled mass spectrometer (MC-ICP-MS) (Shen et al., 2012) at the High-Precision Mass

219 Spectrometry and Environment Change Laboratory (HISPEC), National Taiwan University, and (2)

220 on α-spectrometer at the Laboratory of Environmental and Isotopic Geochemistry, Department of

221 Sciences, Roma Tre University, Italy. For MC-ICP-MS dating, we covered about 0.05 g of each

222 sample with H_2O and dissolved it gradually with double distilled 14 N HNO_3. After dissolution, we

223 added a ^{229}Th–^{233}U–^{236}U spike (Shen et al., 2003) to the sample, followed by 10 drops of $HClO_4$ to

224 decompose organic matter. We followed the chemical procedure described in Shen et al. (2003) for

225 the separation of uranium and thorium. Detailed instrumental analysis is given in Shen et al. (2012).

226 Age correction was calculated using an estimated atomic $^{230}Th/^{232}Th$ ratio of 4±2 x 10^{-6}. The value

227 is the one typical for a material at secular equilibrium with the crustal $^{232}Th/^{238}U$ value of 3.8 and an

228 arbitrarily assumed 50% error. Half-lives of U-Th nuclides used for age calculation with 2-sigma

229 uncertainty are from Cheng et al. (2013). For α-spectrometry dating, samples were cut with a

230 diamond saw and ultrasonically washed in deionized water. About 60 g of each prepared sample

231 were thus dissolved in 7 N HNO_3 and filtered to separate leachates from insoluble residue. The

232 leachates were heated to 200 °C after adding a few millilitres of hydrogen peroxide to annihilate

233 organic matter, then spiked with a $^{228}Th/^{232}U$ tracer. U and Th were extracted according to Edwards

234 et al. (1987), then analysed through alpha-counting using high-resolution ion-implanted Ortec

235 silicon-surface barrier detectors. For samples with a $^{230}Th/^{232}Th$ activity ratio higher than 80 (with

236 insignificant non-radiogenic ^{230}Th), ages were determined using the measured $^{230}Th/^{234}U$ and

237 $^{234}U/^{238}U$ activity ratio. Sample ages characterized by a $^{230}Th/^{232}Th$ activity ratio less than or equal

238 to 80 indicating the presence of non-radiogenic (detrital) ^{230}Th required a correction based on the

239 assumption of an average $^{230}Th/^{232}Th$ activity ratio of 0.85 ± 0.36 for all detrital Th (Wedepohl,

240 1995). All ages were finally calculated using ISOPLOT (Ludwig, 2003) with errors expressed as

241 ±1σ.

242   Samples for geochemical analysis were obtained by micro-drilling. Carbon and oxygen

243 isotope analyses of 50 samples from the WFS (Table A1) were carried out at the Istituto di Geologia

244 Ambientale e Geoingegneria of the Consiglio Nazionale delle Ricerche (Rome, Italy), by acid

245 digestion at 72°C using a Thermo Fisher Scientific Gasbench II coupled to a Delta+ mass

246 spectrometer. Approximately 120 μg of powder was weighted in duplicate. Standardisation to the

247 V-PDB scale was accomplished with three internal standards MC-200, $CaCO_3$ (Merck CCM) and

248 Solnhofen limestone (SLNF) calibrated against the international references NBS18 and NBS19.

249 Oxygen and carbon isotopes are reported with respect to the Vienna Pee Dee Belemnite standard

250 (V-PDB).

The clumped isotope compositions of the carbonates were determined at ETH Zürich using a Thermo Fisher Scientific 253Plus mass spectrometer coupled to a Kiel IV carbonate preparation device, following the method described in Schmid and Bernasconi (2010), Meckler et al. (2014), and Müller et al. (2017). The Kiel IV device included a PoraPakQ trap kept at - 40°C to eliminate potential organic contaminants. Prior to each sample run, the pressure-dependent backgrounds were determined on all beams to correct for non-linearity effects in the mass spectrometer according to Bernasconi et al. (2013). During each run, 20 replicates of 100-120 µg of different samples and 5 replicates of each of the two carbonate standards ETH-1, ETH-2, and 10 of ETH-3 were analysed in LIDI mode. Data processing was carried out with the software Easotope (John and Bowen, 2016) using the IUPAC parameters for 17O correction as suggested by Daeron et al. (2016). The data are reported in the Intercarb Carbon dioxide equilibration scale (I-CDES) (Bernasconi et al. 2021) and the temperatures of formation were calculated with the Anderson et al. (2021) calibration. The oxygen isotopic composition ($\delta^{18}O_{fluid}$) of the fluids was calculated using the calibration of Kim and O'Neil (1997).

4. Results

4.1. Outcrop scale structures

Near Roccacasale (Fig. 2e), the WFS cuts through a sequence of Sinemurian dolomitised limestones. There, the WFS consists of multiple NW-SE-striking fault strands dipping moderately (30°-50°) to SW, typically associated with dm-to-m-thick damage zones (Fig. 3a). The main slip surface, which accommodates the most important offset, commonly show a planar morphology and hosts slickenlines, provided by abrasion striae and rare calcite fibres (Fig. 3b). Slickenlines show pitch values generally around 80° and 100° (Fig. 3b), indicative of nearly pure dip-slip kinematics. Stratigraphic offset, synthetic shears, dragging of the bedding at the fault surfaces, and calcite fibres indicate normal-sense movement.

The main slip surface is associated with a metre-thick damage zone and dm-thick fault core at the footwall (Fig. 3c,d; see also Ferraro et al., 2018). The damage zone is characterised by dm-thick lenses of either massive or foliated cataclasite (Fig. 3e). Cataclasites wrap around dm-to-half metre-thick lithons of almost undeformed limestone. The boundaries between the cataclasite lenses are commonly marked by mm-thick, subsidiary fault zones, synthetic to the main slip surface (Fig. 3e). Massive cataclasites are characterised by matrix-clast proportion >50% and clasts are sub-angular to sub-rounded and up to 1 cm-wide. Foliated cataclasites are characterised by faint layers

284   with different grain size. Approaching the main slip surfaces, matrix becomes extremely dominant

285   and defines centimetre-thick layers of ultra-cataclasite (Fig. 3e; see also Coppola et al., 2021).

286   High angle (dip > 55°; insert in Fig. 3a) faults have been mostly observed at the hanging

287   wall of the main slip surface (Fig. 4a-c). These fault strands are characterised by roughly planar slip

288   surfaces (in section view) dipping to the W-WSW (Fig. 4a,b). The high-angle faults systematically

289   cut and displace the main slip surface, producing centimetre-to-decimetre down-dip offsets and

290   incipient rigid fault block rotation (Fig. 4b,c). They are commonly accompanied by sets of fault-

291   parallel joints and lenses of proto-cataclasites, defining centimetre-thick damage zones.

292   Carbonate mineralisations occur on the main slip surfaces and on the high-angle normal

293   faults (Fig. 4d-h). The main mineralisation is up to 10 cm-thick and consists of a layered calcite,

294   found in the immediate hanging wall of the main slip surface (Fig. 4c,d). In section view, layering is

295   dominantly plane-parallel, although thickness variations from few centimetres up to 15 cm, and

296   pinch-out geometry on older strata can be locally recognised (Fig. 4e,f). When associated with high-

297   angle faults, carbonate mineralisations consist of up to one cm-thick layers of fine grained calcite

298   lying atop striated surfaces (Fig. 4g,h). Layering in these mineralisations is mm-thick, dominantly

299   plane and parallel to the fault surfaces.

300

301   *4.2. Meso- to micro-scale structures*

302   The mineralisations consist of the rhythmic layering of mm-thick laminae and sparitic veins

303   (Figs. 5a,b and SM1a-e). The laminae, which often appears as alabaster-like translucent deposit of

304   fine-grained and massive calcite, are fault-parallel and often characterised by variation in thickness

305   and marked by change in colour from whitish to light brown (Figs. 5a and SM1a,d). Layers of fine-

306   grained calcite are locally intercalated by mm-to-cm-thick pockets of sedimentary breccias,

307   probably filling voids of karst origin. The fabric of the breccia consists of a chaotic distribution of

308   up to 1-cm large limestone clasts (i.e., protolith) mixed with other carbonate fragments deriving

309   from the previous cataclasite (Fig. 5a). The sparitic veins are up to one cm-thick, poorly- to non-

310   porous and are disposed parallel to the fault surface (Figs. 5a,b; SM1a,b,e). Macroscopically, veins

311   show fan-shaped morphology of elongated crystals, which provides unequivocal evidence on the

312   growth direction.

313   At the microscale, cataclasites show sub-rounded clasts, with increasing roundness

314   associated with decreasing particle size (Figs. 5d-f and 6a). The main structural characteristics are:

315   (i) sub-angular clasts fragmented at their edges and clasts showing internal set of polygonal

316 fractures (Fig. 5e,f, 6a,b,d, SM2a-c,g); (ii) truncated clasts by sharp slip surfaces (Fig. 6c); (iii)

317 traces of permeating fluid within the fine-grained matrix and mantling the carbonate clasts (Fig.

318 6d); (iv) sigmoidal foliation in proximity of the main slip surfaces (Figs. 5d; SM2d; SM3l,m).

319 Cathodoluminescence analysis reveals that the convolute structures are characterised by an overall

320 bright-purple colour, distinctively brighter than the calcite of both the fine-grained matrix and the

321 clasts (Fig. 6e).

322   Carbonate laminae and sparitic veins grew from a slip surface that truncates the cataclasite

323 (Figs. 6f, SM2a-f, SM3). While the laminae are characterised by fine-grained, dirty calcite mixed

324 with clay particles (Fig. 6j), the sparitic veins show an internal fibrous texture with crystal growth

325 direction roughly perpendicular to the vein wall (Fig. 6f). The calcite crystal tends to form vein-

326 normal elongated fan-shaped patterns, which are indicative of the vein growth direction and sense.

327 We observed both downward and upward growth patterns, with crystal that converge toward the

328 medial line of the veins, documenting a general syntaxial grow mechanism (Fig. 6f,k; SM3d,g).

329 Cathodoluminescence shows that this calcite is characterised by dull brown/black colour,

330 particularly darker than the calcite occurring within the cataclasite (Fig. 6g).

331   The mineralisations are locally reworked by fracturing and cataclasis to form new clasts

332 (Figs. 6h,i; SM2c-e; SM3h-m). They are affected by micro-joints producing micrometer

333 displacements or display deformation including sigmoidal foliation-like structure embedded in

334 minor slip surfaces (Fig. SM2d; SM3l,m). Reworked mineralisations are often surrounded by

335 secondary micro-crystalline calcite cements with a purple cathodoluminescence like the calcite in

336 the fine-grained matrix. Strips of protocataclasites are locally preserved or bracketed within

337 multiple generations of mineralisations (Fig. 6j,k). Bands parallel to the slip surface and formed by

338 cataclasites alternating with highly fractured mineralisations are observed within veins and laminae

339 (Fig. SM3). The boundaries between cataclasites and mineralisation are often represented by slip

340 surfaces or extensional fractures (Figs. 5a,c; SM2c-f) and some mineralisations are flattened and

341 truncated along the slip surface (Fig. SM3f,g).

342

4.3. U-Th geochronology

344   We dated calcites from nine mineralisations (Table 2). Dated samples are characterised by a

345 roughly homogeneous ^{230}Th/^{238}U activity ratio (between 0.87 and 0.93) and a highly variable

346 ^{230}Th/^{232}Th activity ratio (between 243.2 ± 2.5 and 18969 ± 315) (Table 2). Collectively, samples

347 dated by the MC-ICP-MS method (samples M4G, M4H, M4H2, M4HW, M4F1, M4i) show ages

348   between 190 and 270 ka, with 2σ errors < 7 ka. The sample dated by α-spectrometry (sample M4e)

349   shows a mean age of 178 ka and larger 1σ error of +39 and -30 ka.

350   In the following, we detail the obtained ages with respect to the structural site of the

351   selected sample at the studied outcrop (Figs. 5, 7 and SM1). The oldest age (267.9 ± 6.1 ka) has

352   been obtained from sample M4H, which is a carbonate mineralisation collected from the main slip

353   surface. Three progressively younger ages (257.4 ± 4.3 ka; 246.6 ± 2.5 ka; 230.3 ± 2.0 ka) have

354   been obtained from three generations of calcite of sample M4G (bottom-to-top: M4G3, M4G2,

355   M4G1, respectively), a dm-thick mineralisation collected along the main slip surface (Fig. 5a).

356   Sample M4e (178 +39/-30 ka) has been also collected from the same main slip surface of M4G. A

357   cluster of similar ages have been obtained from samples M4H2 (218.3 ± 3.7 ka), M4HW (215.8 ±

358   6.7 ka), and M4F1 (214.9 ± 2.1 ka). Sample M4H2 is from the lower part of the M4H

359   mineralisation; sample M4F1 are from the upward portion of the M4G mineralisation; sample

360   M4HW is from the top of the sample M4e. Finally, the youngest age (189.4 ± 2.5 ka) has been

361   obtained from sample M4i, from a high angle normal fault crosscutting the main fault plane (Fig.

362   7).

363

364   ### 4.4. Stable carbon and oxygen and clumped isotopes

365   The analysed samples (carbonate clast in cataclasite, fine-grained matrix in cataclasite,

366   sedimentary breccias embedded within the mineralisation, and carbonate mineralisations deposited

367   on fault surfaces) can be grouped in different endmembers showing distinct isotope signatures (Fig.

368   8). The clasts in cataclasites are characterised by $\delta^{13}C$ ranging from 1.40‰ and 2.38‰ and $\delta^{18}O$

369   between -0.43‰ and -1.32‰ typical of marine limestones. Three samples of the fine-grained

370   cataclasite matrix are characterised by $\delta^{13}C$ between 0.61‰ and 0.19‰ and $\delta^{18}O$ between -1.83‰

371   and -2.08‰ whereas one has much more negative $\delta^{18}O$ (-9.04‰) and $\delta^{13}C$ (-8.67‰). Two samples

372   of sedimentary breccias are characterised by negative $\delta^{18}O$ between -3.04‰ and -3.33‰ and $\delta^{13}C$

373   between -1.13‰ and -1.35‰. Finally, the samples of carbonate mineralisations are characterised by

374   negative values of both $\delta^{18}O$ (between -7.37‰ and -11.65‰) and $\delta^{13}C$ (between -7.14‰ and -

375   10.46‰).

376   Clumped-isotope data from 6 carbonate mineralisations yield Δ47 values in a narrow range

377   between 0.552‰ and 0.600‰ (I-CDES) (Table A2). These values correspond to temperatures

378   between 40 ±7 °C and 23 ±4 °C. Calcite from M4G mineralisations dated between ~257 and ~230

379   ka (samples M4G_1b; M4G_1e; M4G_2a; M4G_2b; M4G_3c) precipitated at ~24-28 °C (95%

380   confidence level between ±3 and ±9 °C). Calcite from younger M4F1 mineralisation (dated at

381 ~215) precipitated at 40±11 °C (sample M4F1_2). Finally, a cataclasite (samples M4G_5N) and the

382 host rock clast (M4HW_1N) yielded temperatures of 41-45 °C (±7 °C, 95% confidence level).

383   The calculated $\delta^{18}O$ of the fluids from the 6 mineralisation samples range from -9.3 to -3 ‰

384 (VSMOW) reflecting a dominant meteoric water signal. The calculated fluids for the cataclasite and

385 host rock clast reflect a combination of the original marine carbonate components and the

386 composition of the fluids during burial diagenesis, and are not relevant for the further discussion of

387 the vein fluids.

388

389

5. Discussion

5.1. Structural interpretation

392   Previous structural studies of the MMFS documented fault rock heterogeneities (inner fault

393 core, outer fault core, damage zones, principal slip surfaces) developed via multiple deformation

394 phases of the Meso-Cenozoic carbonate bedrocks (Ferraro et al., 2018; 2019). Intense shear strain

395 localisation occurred along fluid-assisted co-seismic ultracataclastic layers (Coppola et al., 2021).

396 By integrating the insights from these studies with our data, we refine our understanding of the

397 structural permeability along the MMFS (Fig. 9a), which is governed by a continuous interplay

398 between tectonic deformation, fluid circulation and mineralisation. Our meso-to-microscale

399 observation can guide to a scenario of polyphasic permeability evolution from deep to shallow

400 conditions (Fig. 9b).

401   The early structural permeability formed in conditions of confined pressure corresponding to

402 the depth from which the main slip surface exhumed (< 3 km; Ghisetti and Vezzani, 2000; Coppola

403 et al., 2021). The early structural permeability (t_n in Fig. 9b) is controlled by the spatial distribution

404 of structures associated with formation of the damage zone and the fault core at the expense of

405 carbonate bedrock (Fig. 3c,d; Ferraro et al., 2018). The transition from the damage zone to the fault

406 core is attested by a strong grain size reduction and the occurrence of foliated cataclasites, which

407 progressively replace the massive ones in the damage zone proximal to the fault core (Figs. 3e, 4f).

408 Cataclasis is the main deformation mechanism steering significant deformation in the damage zone

409 and the fault core (Fig. 3c-e). Rock comminution and clast roundness in cataclasites is assisted by

410 chipping at the edges of the sub-angular clasts, as well as intergranular fracturing contributes to

411 grain size reduction in larger clasts (Figs. 5, 6a,d, SM2f; Billi, 2010 and references therein).

412 Carbonate clasts are commonly truncated by subsidiary slip surfaces and the fine cataclasite matrix

413 is permeated by fluidised ultra-fine material (Fig. 6c,e). As already argued by Coppola et al. (2021),

414 we consider these microstructural features as evidence for coseismic rupturing, comparable to

415 potential seismic markers documented from faulted carbonates within tectonic domains (Hadizadeh,

416 1994; Smith et al., 2011; Fondriest et al., 2012; Tesei et al., 2013; Smeraglia et al., 2016; Delle

417 Piane et al., 2017).

418 The subsequent structural permeability (t_{n+nx} in Fig. 9b) formed at shallower crustal

419 conditions and was connected to the development of sharp, discrete slip surfaces cutting through the

420 cataclastic fabric in both the damage zone and the fault core. Ferraro et al. (2018) document matrix-

421 supported textures for these slip surfaces, developed in the latest stages of fault exhumation. The

422 main slip surface occurs within the fault core and corresponds to the striated one atop the proximal

423 slip zone (of co-seismic origin) of Coppola et al. (2021) (Fig. 9c). This suggests a mechanical

424 scenario of progressive fault narrowing through multiple episodes of fabric reworking and shear

425 strain localisation (Smith et al., 2011; Smeraglia et al., 2018; Vignaroli et al., 2020b). The

426 mineralisations are exclusively localised along the main slip surfaces and on the slip surface of the

427 high-angle fault (Fig. 9a), not associated with a system of veins in the damage zone. We propose

428 that the fault surfaces acted as localised, fault-parallel conduits (Caine et al., 1996) and the fluid

429 circulation channelised within the fault core during reactivation and dilatancy of the slip surfaces

430 (Fig. 9b). The combination between faulting and dilatancy during creation of the structural

431 permeability is attested by: (i) carbonate mineralisation within cataclasite in dilatant jog (Fig. 4d);

432 (ii) fan-shaped crystals growth in veins documenting a general syntaxial grow mechanism (Figs.

433 6f,k; SM3); (iii) reworked carbonate mineralisations often fractured and cut by slip surfaces (Figs.

434 SM2a-f; SM3a); (iv) carbonate mineralisations incorporated within the underlying cataclasites or

435 embedded as pockets in protocataclasite or breccias (Figs. 5; 6; SM2; SM3); (v) bands parallel to the

436 slip surfaces made of protolith cataclasite alternating with highly fractured mineralisations (Fig.

437 SM3); and (vi) sigmoidal foliation-like structure embedded in minor slip surfaces within the

438 mineralisations (Figs. SM2d; SM3l,m). The (re)activation of main slip surfaces occurred during the

439 progressive exhumation of the fault core-damage zone formed at deeper structural levels.

440 Considering the U-Th age range (between 268 and 189 ka) and the Holocene slip rate estimated for

441 the MMFS (0.4-1.1 mm/yr Roberts and Michetti, 2004; Gori et al., 2011), we obtain depths between

442 60 and 300 m below the present-day outcrop elevation (~450 m a.s.l.) for the development of the

443 shallow structural permeability. In this time-dependent conceptual evolution of the structural

444 permeability, the development of the high-angle normal faults crosscutting the main fault core

445 represents the last increment of strain during fault growth and exhumation.

446

5.2. Fluid circulation

The structural interpretation can be integrated with the isotope data (Fig. 8; Table A1) to propose a comprehensive time-dependent scenario for fluid circulation during the progressive exhumation of the MMFS and concomitant subsidence of the Sulmona Basin at its hanging wall (e.g., Miccadei et al., 2002; Gori et al., 2011; Galli et al., 2015; Fig. 9d). The protolith carbonate clasts embedded in cataclasites have the highest isotope values, in the range of unaltered Mesozoic marine carbonates from the central Apennines (e.g., Ghisetti et al. 2001; Agosta and Kirschner 2003; Smeraglia et al., 2016). The cataclasite matrix, representing the early structural permeability, shows more negative isotope values consistent with mixing of marine carbonate particles with calcite precipitated from meteoric waters. As observed in Figure 8, the cataclasites plot on a mixing line between the host rock and the mineralisation.

The mineralisations formed within the shallowest structural permeability show typical carbon and oxygen isotope signatures of calcite precipitated from meteoric waters that gained a significant contribution of respired organic carbon in the soils. The calculated $\delta^{18}O$ of the fluids ranges between -3 and -9‰ (VSMOW) and is like the average composition of rainfall (-7 and -9‰) and slightly enriched with respect to the spring water (-8 and -11‰) in the central Apennines (Minissale, 2004). Fluid temperatures (Table A2) range between 23 and 26° C. These temperatures are, except for a mineralisation dated at 215 ka (Fig. SM1d), warmer than those of spring waters found in the Sulmona Basin (6-15 °C; Barberio et al., 2017) and, in general, for cold springs emerging in central Apennines (e.g., Minissale, 2004). Also, the calculated $\delta^{18}O$ of the fluids are enriched in ^{18}O with respect to the spring waters in the Sulmona Basin (-10 to -11‰; Barberio et al., 2017). We, therefore, infer that syn-tectonic mineralisations occurring along the MMFS could preserve a minimal component of deeper flow, probably from the deeper circulating waters with longer residence time, mixed with the dominant shallow meteoric water circulation. It is noteworthy that the hottest sample at 40° C (M4F1-2; Table A2) yields the least negative calculated $\delta^{18}O$ of the fluids, suggesting a contribution of warmer fluid with a higher oxygen isotope composition resulting from more intense water-rock interaction as observe by Smeraglia et al. (2018) in the Val Roveto Fault (see location in Fig. 2a). These temperatures are comparable with the coldest fluid temperatures (between 32 and 75 °C) estimated for syn-tectonic mineralisations in potentially-seismogenic structures (Smeraglia et al., 2016; 2018) and for tectonically controlled veins in thermogene travertines in central Apennines (e.g., Berardi et al., 2016).

5.3. Implications for long-term fault history

480   The results from this and other studies (e.g., Ferrero et al., 2018; Coppola et al., 2021; Fig.

481   9c) confirm active coseismic rupturing during growing of the MMFS, creating secondary

482   permeability through major fracturing and cataclastic flow, which produced viable structural

483   network for fluid ingress. The U-Th ages spanning the Middle Pleistocene (between 268 and 189

484   ka) represent the first geochronological documentation of the long-term deformation history of the

485   MMFS, constraining the timing of cycles of permeability creation and destruction in response to

486   continuous interplay between brittle deformation and fluid ingress.

487   Our seismic scenario for the MMFS (Fig. 9e) proposes episodes of coseismic failure at

488   depth with faulting and tensile fracturing at shallower crustal levels, where the carbonate

489   mineralisations formed. Coseismic failure at seismogenic depths led to rejuvenation of the fault

490   permeability through the activation/reactivation of slip surfaces at shallower depths, favouring

491   channelised mineralising flow (e.g., Caine et al., 1996; Cox et al., 2001; Rowland and Sibson, 2004;

492   Sibson, 2014). Between successive failure events (interseismic/postseismic stage), shallow fault

493   permeability decreased ever more by carbonate precipitation and progressive sealing of the fault-

494   related structures. We propose that the syn-tectonic mineralisations within the MMFS constitute a

495   record of fault (re)activation and tensile episodes in response to the cyclic stress accumulation that

496   can be used to constrain the age of fluid ingress in response to the seismic failure. U-Th data

497   document activation of faulting/tensile failure in the periods 267, 257, 246, 230, and 215 ka. This

498   suggests a time recurrence in the range of 10-15 ka (Fig. 9e).

499   Our integrated geological model can help to reconstruct the activity of seismogenic master

500   faults of central Apennines, currently primarily constrained by seismic catalogues (e.g., Rovida et

501   al., 2020) and paleoseismological datasets (e.g., Galli et al., 2008), to much longer temporal and

502   spatial scales. Very few studies provided geochronological constraints on neotectonics by dating

503   syn-tectonic mineralisation related to major faults (Fig. 10). Smeraglia et al. (2018) dated four fault-

504   related mineralisations along the Val Roveto Fault (see location in Fig. 2a), which the authors used

505   to constrain fluid migration and mixing during Late Pleistocene multiple displacement episodes and

506   seismic slip along the fault. Vignaroli et al. (2020a) dated fault-related mineralisations along the

507   Amatrice Fault System (see location in Fig. 2a), used to constrain surface rupture and

508   hydrodynamic interconnection with the vadose zone during Middle-Late Pleistocene faulting. While

509   a cyclical reactivation of the MMFS occurred within the Middle Pleistocene between 268 and 189

510   ka, both the Val Roveto Fault and the Amatrice Fault System activated before 290 ka, followed by

511   reactivation in the Late Pleistocene-Early Holocene (Fig. 10).

512   All together, these fault-related mineralisations typify the time of multiple rupture events
513   along major NW-SE-striking normal faults, their reactivation and the recurrence interval connected
514   with their seismic cycle. Such an integrated geological model for seismogenic faults could play a
515   key role in seismic hazard assessment in those areas characterised by the absence of historical
516   seismicity and/or evidence of Mw < 6 paleoearthquakes. Additional studies on similar syn-tectonic
517   mineralisations could make possible to identify cyclical variations in the fluctuation of fluid ingress
518   at greater frequency and, therefore, to provide a viable contribution to the definition of a recurrence
519   pattern on a regional scale.

520

5.4. The paleoclimate influence

522   To understand possible feedback relationships between paleoclimate changes and fault-
523   controlled circulation of mineralising fluids, we compared our ages for the MMFS carbonate
524   mineralisations with U-Th ages obtained for some Quaternary travertines and calcite veins located
525   on the Tyrrhenian margin of the Apennines (Semproniano-Saturnia travertines: Berardi et al., 2016;
526   Vignaroli et al., 2016; Radicofani and Val di Chiana travertines: Brogi et al., 2010; 2012; 2017; Fig.
527   10). We considered major Quaternary paleoclimate indicators determined at both local and regional
528   scale (Fig. 10), the pollen data set from Valle di Castiglione (Tzedakis et al., 2001) located ~100
529   km to the west of the MMFS and the atmospheric CO_2 concentration (Past Interglacial Working
530   Group of PAGES, 2016). We also considered the climate anomalies generated by periodic
531   oscillations of Earth's orbital parameters over the Cenozoic (Zachos et al., 2001; Past Interglacials
532   Working Group of PAGES, 2016).

533   The available U-Th data cover the time spanning from MIS 10 to MIS 5 (MIS: Marine
534   Isotope Stage; Fig. 10). There is a consensus in considering warm and wet (interglacial) conditions
535   as the most favourable for thermogene travertine deposition during late Quaternary time (e.g.,
536   Sturchio et al., 1994; Rihs et al., 2002; Faccenna et al., 2008; Uysal et al., 2009; De Filippis et al.,
537   2013; Priewisch et al., 2014). In this view, the ages obtained for the Semproniano-Saturnia
538   travertines fall within warm and humid climate periods that have been considered as triggers for
539   tectonically controlled fluid discharge along faults (Berardi et al., 2016; Vignaroli et al., 2016). On
540   the other hand, a different pattern has been proposed for the travertines in Radicofani Basin, Val di
541   Chiana Basin and Tiber Valley (Brogi et al., 2010; 2012; 2017; Giustini et al., 2018), suggesting the
542   importance of tectonic activity, rather than climate, to control travertine precipitation during low
543   stand conditions of the water table in dry glacial periods (e.g., Uysal et al., 2009; Özkul et al.,
544   2013). Moreover, some studies documented a correlation between growth phases of surficial

carbonate mineralisation (travertines and veins) and times of cyclical variations of the Earth's orbital characteristics, including the c. 25 ka precessional component that controls high insolation (e.g., Wang et al., 2004; Kampman et al., 2012; De Filippis et al., 2013).

Discarding the sample M4e, due to its rather large error bars, we note that five of MMFS U-Th ages fall within the interglacial period, at 180-245 ka (MIS7 in Fig. 10), while three fall within the glacial period MIS8. Noteworthy, ages within the MIS7 and MIS8 show a preferential correlation with the interstadial events (humid times suggested by the high values of the pollen data set from Valle di Castiglione). This correlation matches with paleoclimate conditions supplying the deposition of the Semproniano-Saturnia thermogene travertines (Berardi et al., 2016; Vignaroli et al., 2016). In addition, over the periods 100-150 and 300-350 ka there is a good correlation between the mean ages of mineralisations from the Val Roveto Fault (s61, s129, s132, s149 in Fig. 10), the Amatrice Fault System (Fven1/2, Fin8 in Fig. 10), and travertines with the rhythmical negative peaks of precession (i.e., conditions of high insolation). Overall, this might suggest that carbonate precipitation in active faults and travertines is sensitive to climate variation, being preferentially facilitated by warm and humid climate conditions characterised by high-stands of the water table. In dryer times, scarce meteoric water supply might not allow the formation of carbonate mineralisations in active tectonic structures. Therefore, the variations in climate-controlled water availability could bias the recorded periodicity of fault activity, as cycles of permeability creation and destruction under dry conditions would not lead to significant mineral precipitation.

6. Conclusions

The structural evolution of the MMFS supports the general scenario of focussed, structurally-controlled fluid flow and mineralisation at shallow depths during fault reactivation. We document multiple events of permeability creation and destruction recording the long-term evolution of the MMFS:

(i) The development of the secondary permeability in the MMFS evolved in space in time from diffuse deformation (at the fault footwall) towards localisation of a narrower fault core and to final (re)activation of discrete slip surfaces in the shallower crustal levels. The latter correspond to a combination of faulting and tensile fracturing, in response to the stress accumulation during its seismic cycle.

(ii)   The hydrodynamic regime permeating the secondary permeability mineralising fluid was dominated by meteoric water circulation at the shallower conditions, where discrete slip surfaces (re)activated.

(iii)   The polyphasic and syn-tectonic mineralisations on the fault surfaces reflect the interaction and feedback among seismically active tectonics and transient circulation of mineralising fluids, likely influenced by paleoclimate oscillations.

(iv)   U-Th dating of the carbonate mineralisations defined the time lapse encompassed in the fault permeability creation/destruction cycles, providing a pilot study to reconstruct the seismic recurrence model at a regional scale.

References

Agosta, F., and Kirschner, D.L., 2003. Fluid conduits in carbonate-hosted seismogenic normal faults of central Italy. J. Geophys. Res. 108, 2221. http://dx.doi.org/10.1029/2002JB002013.

Agosta, F., Mulch, A., Chamberlain, P., and Aydin, A., 2008. Geochemical traces of CO2-rich fluid flow along normal faults in central Italy. Geophys. J. Int., 174, 758–770 doi: 10.1111/j.1365-246X.2008.03792.x.

Amato, A., Azzara, R., Chiarabba, C., Cimini, G.B., Cocco, M., Di Bona, M., Margheriti, L., Mazza, S., Mele, F., Selvaggi, G., Basili, A., Boschi, E., Courboulex, F., Deschamps, A., Gaffet, S., Bittarelli, G., Chiaraluce, L., Piccinini, D., and Ripepe, M., 1998. The 1997 Umbria-Marche, Italy, earthquake sequence; a first look at the main shocks and aftershocks. Geophys. Res. Lett., 25, 2861–2864.

Anderson, N. T., Kelson, J. R., Kele, S., Daëron, M., Bonifacie, M., Horita, J., et al., 2021. A unified clumped isotope thermometer calibration (0.5–1,100°C) using carbonate-based standardization. Geophysical Research Letters, 48, e2020GL092069, https://doi.org/10.1029/2020GL092069.

Barberio, M.D., Barbieri, M., Billi, A., Doglioni, C., Petitta, M., 2017. Hydrogeochemical changes before and during the 2016 Amatrice-Norcia seismic sequence (central Italy). Scientific Reports, 7, 11735, doi:10.1038/s41598-017-11990-8.

Barchi, M.R., De Feyter, A., Magnani, B., Minelli, G., Pialli, G., and Sotera, B., 1998. The structural style of the Umbria-Marche fold and thrust belt. Mem. Soc. Geol. It., 52, p. 557–578.

Berardi, G., Vignaroli, G., Billi, A:, Rossetti, F., Soligo, M., Kele, S., Baykara, M.O., Bernasconi, S.M., Castorina, F., Tecce, F., Shen, C.C., 2016. Growth of a Pleistocene giant carbonate vein and nearby thermogene travertine deposits at Semproniano, southern Tuscany, Italy: Estimate of CO2 leakage. Tectonophysics, 690, 219-239, http://dx.doi.org/10.1016/j.tecto.2016.04.014.

Bernasconi, S. M., Hu, B., Wacker, U., Fiebig, J., Breitenbach, S. F. M., & Rutz, T., 2013. Background effects on Faraday collectors in gas-source mass spectrometry and implications for clumped isotope measurements. Rapid Communications in Mass Spectrometry, 27(5), 603–612. https://doi.org/10.1002/rcm.6490.

Bernasconi, S. M., Daëron, M., Bergmann, K. D., Bonifacie, M., Meckler, A. N., Affek, H. P., et al., 2021. InterCarb: A community effort to improve interlaboratory standardization of the carbonate clumped isotope thermometer using carbonate standards. Geochemistry, Geophysics, Geosystems, 22, e2020GC009588, https://doi.org/10.1029/2020GC009588.

Billi, A., 2010. Microtectonics of low-P low-T carbonate fault rocks. J. Struct. Geol. 32, 1392-1402.

Boccaletti, M., Calamita, F., Deiana, G., Gelati, R., Massari, F., Moratti, G., and Ricci Lucchi, F., 1990. Migrating foredeep-thrust belt systems in the northern Apennines and southern Alps. Palaeogeography, Palaeoclimatology, Palaeoecology, 77, 3-14.

Boncio, P., Galli, P., Naso, G., and Pizzi, A., 2012. Surface fault rupture hazard along normal faults: Insight from the 2009 L'Aquila earthquake (Mw 6.3, central Italy), observations from global normal faulting earthquakes and implications for earthquake fault zoning. Bull. Seismol. Soc. Am., 102, 918–935.

Boncio, P., Lavecchia, G., Milana, G., and Rozzi, B., 2004. Seismogenesis in Central Apennines, Italy: an integrated analysis of minor earthquake sequences and structural data in the Amatrice-Campotosto area. Ann. Geophys.-Italy, 47, 1723-1742.

Braathen, A., Osmundsen, P. T., Gabrielsen, R. H., 2004. Dynamic development of fault rocks in a crustal-scale detachment: An example from western Norway. Tectonics 23, TC4010, doi: 10.1029/2003TC001558.

644 Brogi, A., Capezzuoli, E., Aquè, R., Branca, M., and Voltaggio, M., 2010. Studying travertines for neotectonics
645 investigations: Middle–Late Pleistocene syn-tectonic travertine deposition at Serre di Rapolano
646 (Northern Apennines, Italy). International Journal of Earth Sciences, 99, 1383–1398, doi:
647 10.1007/s00531-009-0456-y.

648 Brogi, A., Capezzuoli, E., Buracchi, E., and Branca, M., 2012. Tectonic control on travertine and calcareous
649 tufa deposition in a low-temperature geothermal system (Sarteano, central Italy). Journal of the
650 Geological Society, London, 169, 461–476, doi: 10 .1144/0016 -76492011 -137.

651 Brogi, A., Capezzuoli, E., Kele, S., Baykara M.O., Shen, C.C., 2017. Key travertine tectofacies for
652 neotectonics and palaeoseismicity reconstruction: effects of hydrothermal overpressured fluid injection.
653 Journal of the Geological Society, London, https://doi.org/10.1144/jgs2016-124.

654 Caine J.S., Evans J.P., Forster C.B., 1996. Fault zone architecture and permeability structure. Geology, 24,
655 1025-1028.

656 Carminati, E., Lustrino, M., Cuffaro, M., & Doglioni, C., 2010. Tectonics, magmatism and geodynamics of
657 Italy: what we know and what we imagine. J. Virtual Explor., 36(8), 10-3809.

658 Cavinato, G.P., and De Celles, P.G., 1999. Extensional basins in the tectonically bimodal central Apennines
659 fold-thrust belt, Italy: Response to corner flow above a subducting slab in retrograde motion. Geology,
660 27, 955–958, doi: 10 .1130 /0091 -7613.

661 Cavinato, G.P., Carusi, C., Dall'Asta, M., Miccadei, E., and Piacentini, T., 2002. Sedimentary and tectonic
662 evolution of Plio-Pleistocene alluvial and lacustrine deposits of Fucino Basin (central Italy).
663 Sedimentary Geology, 148, 29-59, doi: 10.1016/S0037-0738(01)00209-3.

664 Cello, G., Mazzoli, S., Tondi, E., and Turco, E., 1997. Active tectonics in the central Apennines and possible
665 implications for seismic hazard analysis in peninsular Italy. Tectonophysics, 272, 43–68,
666 doi:10.1016/S0040-1951(96)00275-2.

667 Cheng, H., Edwards, R. L., Shen, C.-C., Polyak, V.J., Asmerom, Y., Woodhead, J., Hellstrom, J., Wang, Y.,
668 Kong, X., and Spötl, C., 2013. Improvements in ^{230}Th dating, ^{230}Th and ^{234}U half-life values, and U-Th
669 isotopic measurements by multi-collector inductively coupled plasma mass spectroscopy. Earth Planet.
670 Sc. Lett., 371-372, 82-91, 10.1016/j.epsl.2013.04.006.

671 Chiarabba, C., et al., 2009. The 2009 L'Aquila (central Italy) Mw 6.3 earthquake: Main shock and aftershocks,
672 Geophys. Res. Lett., 36, L18308, doi:10.1029/2009GL039627.

673 Chiaraluce, L., Di Stefano, R., Tinti, E., Scognamiglio, L., Michele, M., Casarotti, E., Cattaneo, M., De Gori,
674 P., Chiarabba, C., Monachesi, G., Lombardi, A., Valoroso, L., Latorre, D., and Marzorati, S., 2017. The
675 2016 Central Italy Seismic Sequence: A First Look at the Mainshocks, Aftershocks, and Source Models.
676 Seismol. Res. Lett., 88/3, 757-771, doi: 10.1785/0220160221.

677 Collettini, C., Viti, C., Tesei, T., Mollo, S., 2013. Thermal decomposition along natural carbonate faults during
678 earthquakes. Geology 41, 927-930.

679 Conti, A., Turpin, L., Polino, R., Mattei, M., and Zuppi, G.M., 2001. The relationship between evolution of
680 fluid chemistry and the style of brittle deformation: examples from the Northern Apennines (Italy).
681 Tectonophysics, 330, 103-117.

682 Coppola, M., Correale, A., Barberio, M.D., Billi, A., Cavallo, A., Fondriest, M., Nazzari, M., Paonita, A.,
683 Romano, C., Stagno, V., Viti, C., Vona, A., 2021. Meso- to nano-scale evidence of fluid-assisted co-
684 seismic slip along the normal Mt. Morrone Fault, Italy: Implications for earthquake hydrogeochemical
685 precursors. Earth Planet. Sc. Lett., 568, https://doi.org/10.1016/j.epsl.2021.117010.

Cosentino, D., Cipollari, P., Marsili, P., and Scrocca, D., 2010. Geology of the central Apennines: a regional review. In: Beltrando M., Peccerillo A., Mattei M., Conticelli S., and Doglioni C. (eds.), J. Virtual Explor., 36, 11, doi:10.3809/jvirtex.2009.00223.

Cosentino D., Asti R., Nocentini M., Gliozzi E., Kotsakis T., Mattei M., Esu D., Spadi M., Tallini M., Cifelli F., Pennacchioni M., Cavuoto G., Di Fiore V., 2017. New insights into the onset and evolution of the central Apennine extensional intermontane basins based on the tectonically active L'Aquila Basin (central Italy). Geol. Soc. Am. Bull., 129, 9/10, 1314–1336, https://doi.org/10.1130/B31679.1.

Cowie, P.A.. Phillips, R.J., Roberts, G.P., McCaffrey, K., Zijerveld, L.J.J., Gregory, L.C., Faure Walker, J., Wedmore, L.N.J., Dunai, T.J., Binnie, S.A., Freeman, S.P.H.T., Wilcken, K., Shanks, R.P., Huismans, R.S., Papanikolaou, I., Michetti, A.M., Wilkinson, M., 2017. Orogen-scale uplift in the central Italian Apennines drives episodic behaviour of earthquake faults. Sci Rep 7, 44858 (2017). https://doi.org/10.1038/srep44858.

Cox, S.F., 2010. The application of failure mode diagrams for exploring the roles of fluid pressure and stress states in controlling styles of fracture-controlled permeability enhancement in faults and shear zones. Geofluids, 10, 217–233 doi: 10.1111/j.1468-8123.2010.00281.x

Cox, S.F., Knackstedt, M.A., Braun, J., 2001. Principles of structural controls on permeability and fluid flow in hydrothermal systems. Rev. Econ. Geol. 14, 1-24.

Curzi, M., Bernasconi, S.M., Billi, A., Boschi, C., Aldega, L., Franchini, S., Albert, R., Gerdes, A., Barberio, M.D., Looser, N., Carminati, E., 2021. U-Pb age of the 2016 Amatrice earthquake causative fault (Mt. Gorzano, Italy) and paleo-fluid circulation during seismic cycles inferred from inter- and co-seismic calcite. Tectonophysics, 819, https://doi.org/10.1016/j.tecto.2021.229076.

D'Agostino, N., Mantenuto, S., D'Anastasio, E., Giuliani, R., Mattone, M., Calcaterra, S., Gambino, P., Bonci, L., 2011. Evidence for localized active extension in the central Apennines (Italy) from global positioning system observations. Geology, 39, 291–294, doi: 10.1130/G31796.1.

Daëron, M., Blamart, D., Peral, M., & Affek, H. P., 2016. Absolute isotopic abundance ratios and the accuracy of Δ47 measurements. Chemical Geology, 442, 83–96. https://doi.org/10.1016/j.chemgeo.2016.08.014

De Filippis, L., Faccenna, C., Billi, A., Anzalone, E., Brilli, M., Soligo, M., and Tuccimei, P., 2013. Plateau versus fissure ridge travertines from Quaternary geothermal springs of Italy and Turkey: Interactions and feedbacks between fluid discharge, paleoclimate, and tectonics. Earth-Science Reviews, 123, 35-52, doi:10.1016/j.earscirev.2013.04.004.

Delle Piane, C., Clennell, M.B., Keller, J.V.A., Giwelli, A., Luzin, V., 2017. Carbonate hosted fault rocks: A review of structural and microstructural characteristic with implications for seismicity in the upper crust. J. Struct. Geol. 103, 17-36, http://dx.doi.org/10.1016/j.jsg.2017.09.003.

Dewey, J. F., 1988. Extensional collapse of orogens. Tectonics, 7, 1123–1139, doi:10.1029/TC007i006p01123.

Dewey, J.F., Helman, M.L., Knott, S.D., Turco, E., and Hutton, D.H.W., 1989. Kinematics of the western Mediterranean: Geological Society of London Special Publication, 45, 265-283.

Doglioni, C., Barba, S., Carminati, E., Riguzzi, F., 2014. Fault on-off versus coseismic fluids reaction. Geosci. Front. 5, 767–780. http://dx.doi.org/10.1016/j.gsf.2013.08.004.

Edwards, R.L., Chen, J.H., Wasserburg, G.J., 1987, ^{238}U–^{234}U–^{230}Th systematics and the precise measurement of time over the last 500,000 years. Earth Planet. Sc. Lett., 81, 175-192.

Faccenna, C., Becker, T. W., Lucente, F. P., Jolivet, L., & Rossetti, F., 2001. History of subduction and back arc extension in the Central Mediterranean. Geophys. J. Int., 145(3), 809-820.

729   Faccenna, C., Mattei, M., Funiciello, R., & Jolivet, L., 1997. Styles of back- arc extension in the central
730   Mediterranean. Terra Nova, 9(3), 126-130.

731   Faccenna, C., Soligo, M., Billi, A., De Filippis, L., Funiciello, R., Rossetti, C., and Tuccimei, P., 2008. Late
732   Pleistocene depositional cycles of the Lapis Tiburtinus travertine (Tivoli, central Italy): Possible
733   influence of climate and fault activity. Global and Planetary Change, 63, 299–308, doi: 10 .1016 /j
734   .gloplacha .2008 .06 .006.

735   Faure Walker, J. P., Roberts, G. P., Sammonds, P. R., and Cowie, P. A., 2010. Comparison of earthquake
736   strains over 10^2 and 10^4 year timescales: insights into variability in the seismic cycle in the central
737   Apennines, Italy. J. Geophys. Res. 115:B10418. doi: 10.1029/2009JB006462.

738   Ferraro, F., Grieco, D.S., Agosta, F., Prosser, G., 2018. Space-time evolution of cataclasis in carbonate fault
739   zones. J. Struct. Geol., 110, 45-64, https://doi.org/10.1016/j.jsg.2018.02.007.

740   Ferraro, F., Agosta, F., Ukar, E., Grieco, D.S., Cavalcante, F., Belviso, C., Prosser, G., 2019. Structural
741   diagenesis of carbonate fault rocks exhumed from shallow crustal depths: An example from the central-
742   southern Apennines, Italy. J. Struct. Geol., 122, 58-80, https://doi.org/10.1016/j.jsg.2019.02.008.

743   Fondriest, M., Smith, S.A.F., Di Toro, G., Zampieri, D., Mittempergher, S., 2012. Fault zone structure and
744   seismic slip localization in dolostones, an example from the Southern Alps, Italy. J. Struct. Geol. 45, 52-
745   67, http://dx.doi.org/10.1016/j.jsg.2012.06.014.

746   Galadini, F., and Galli, P., 2000. Active tectonics in the central Apennines (Italy)-input data for seismic hazard
747   assessment. Nat. Hazards 22, 225–270.

748   Galadini, F., and P. Galli, 2001. Archaeoseismology in Italy: Case studies and implications on long-term
749   seismicity. J. Earthq. Eng.. 5, 35-68.

750   Galadini, F., and Messina, P., 2004. Early–middle Pleistocene eastward migration of the Abruzzi Apennine
751   (central Italy) extensional domain. J. Geodyn. 37, 57–81.

752   Galli, P., Galadini, F., and Pantosti, D., 2008. Twenty years of paleoseismology in Italy. Earth Sci. Rev. 88,
753   89–117. doi: 10.1016/j.earscirev.2008.01.001.

754   Galli, P., Galderisi, A., Ilardo, I., Piscitelli, S., Scionti, V., Bellanova, J., Calzoni, F., 2018. Holocene
755   paleoseismology of the Norcia fault system (Central Italy). Tectonophysics, 745, 154–169,
756   https://doi.org/10.1016/j.tecto.2018.08.008.

757   Galli, P., Galderisi, A., Peronace, E., Giaccio, B., Hajdas, I., Messina, P., et al., 2019. The awakening of the
758   dormant Mount Vettore fault (2016 central Italy earthquake, Mw 6.6): Paleoseismic clues on its
759   millennial silences. Tectonics, 38, 687- 705. https://doi.org/10.1029/2018TC005326.

760   Galli, P., Giaccio, B., Peronace, E., Messina, P., 2015. Holocene Paleoearthquakes and Early–Late Pleistocene
761   Slip Rate on the Sulmona Fault (Central Apeninnes, Italy). Bull. Seism. Soc. Am., 105, 1-13, doi:
762   10.1785/0120140029.

763   Ghisetti, F., Kirschner, D.L., Vezzani, L., and Agosta, F., 2001. Stable isotope evidence for contrasting
764   paleofiuid circulation in thrust faults and normal faults of the central Apennines, Italy. J. Geophys. Res.,
765   106, 8811-8825.

766   Ghisetti, F., and Vezzani, L., 2000. Modalità di riattivazione, circolazione dei fluidi e rottura sismica di alcune
767   delle principali faglie normali nelle zone esterne dell'Appennino centrale. In: Le Ricerche del GNDT
768   nel Campo della Pericolosità Sismica (1996–1999). CNR, Roma, pp. 193–202.

769   Ghisetti, F., and L. Vezzani, 2002. Normal faulting, transcrustal permeability and seismogenesis in the
770   Apennines (Italy), Tectonophysics, 348, 155–168, doi:10.1016/S0040-1951(01)00254-2.

771 Giaccio B., Galli P., Messina P., Peronace E., Scardia G., Sottili G., Sposato A., Chiarini E., Jicha B., Silvestri
772   S., 2012. Fault and basin depocentre migration over the last 2 Ma in the L'Aquila 2009 earthquake
773   region, central Italian Apennines. Quaternary Sci. Rev., 56, 69-88, doi:10.1016/j.quascirev.2012.08.016.

774 Giaccio, B., Messina, P., Sposato, A., Voltaggio, M., Zanchetta, G., Galadini F., Gori, S., Santacroce, R., 2009.
775   Tephra layers from Holocene lake sediments of the Sulmona basin, central Italy: Implications for
776   volcanic activity in peninsular Italy and tephrostratigraphy in the central Mediterranean area. Quaternary
777   Sci. Rev., 28, 2710-2733.

778 Giustini, F., Brilli, M. & Mancini, M., 2018. Geochemical study of travertines along middle-lower Tiber valley
779   (central Italy): genesis, palaeo-environmental and tectonic implications. Int. J. Earth Sci., 107, 1321–
780   1342, doi.org/10.1007/s00531-017-1535-0.

781 Gori, S., Falcucci, E., Dramis, F., Galadini, F., Galli, P., Giaccio, B., Messina, P., Pizzi, A., Sposato, A.,
782   Cosentino, D., 2014. Deep-seated gravitational slope deformation, large-scale rock failure, and active
783   normal faulting along Mt. Morrone (Sulmona basin, Central Italy): Geomorphological and
784   paleoseismological   analyses.   Geomorphology,   208,   88-101,
785   http://dx.doi.org/10.1016/j.geomorph.2013.11.017.

786 Gori, S., Giaccio, B., Galadini, F., Falcucci, E.,Messina, P., Sposato, A., Dramis, F., 2011. Active normal
787   faulting along the Mt. Morrone south-western slopes (central Apennines, Italy). Int. J. Earth Sci., 100,
788   157–171.

789 Hadizadeh, J., 1994. Interaction of Cataclasis and Pressure Solution in a Low-temperature Carbonate Shear
790   Zone. Pure Appl. Geophys. 143, I/2/3, 255-280.

791 Hickman, S., Sibson, R., Bruhn, R., 1995. Introduction to special section: mechanical involvement of fluids in
792   faulting. J. Geophys. Res. 100, 12831–12840.

793 Hiess, J., Condon, D. J., McLean, N. and Noble, S. R., 2012. $^{238}U/^{235}U$ systematics in terrestrial uranium-
794   bearing minerals. Science, 355, 1610-1614.

795 Iezzi, F., Roberts, G., Faure Walker, J., and Papanikolaou, I., 2019. Occurrence of partial and total coseismic
796   ruptures of segmented normal fault systems: insights from the Central Apennines, Italy. J. Struc. Geol.
797   126, 83–99, doi: 10.1016/j.jsg.2019.05.003.

798 Jaffey, A. H., Flynn, K. F., Glendenin, L. E., Bentley, W. C., Essling, A. M., 1971. Precision measurement of
799   half-lives and specific activities of ^{235}U and ^{238}U. Phys. Rev., C 4, 1889-1906.

800 John, C.M., and Bowen, D., 2016, Community Software for Challenging Isotope Analysis: First Applications
801   of 'Easotope' to Clumped Isotopes. Rapid communications in Mass Spectrometry, 30, 2285– 2300, doi:
802   10.1002/rcm.7720.

803 Kampman, N., Burnside, N.M., Shipton, Z.K., Chapman, H.J., Nicholl, J.A., Ellam, R.M., and Bickle, M.J.,
804   2012. Pulses of carbon dioxide emissions from intracrustal faults following climatic warming. Nature
805   Geoscience, 5, 352-358, doi:10.1038/ngeo1451.

806 Kim S.T. and O'Neil, J.R., 1997. Equilibrium and nonequilibrium oxygen isotope effects in synthetic
807   carbonates. Geochimica et Cosmochimica Acta, 61, 16, 3461-3475.

808 Lanari, R., Faccenna, C., Benedetti, L., Sembroni, A., Bellier, O., Menichelli, I., Primerano, P., Molin, P.,
809   2021. Formation and persistence of extensional internally drained basins: The case of the Fucino basin
810   (Central Apennines, Italy). Tectonics, 40, e2020TC006442, https://doi.org/10.1029/2020TC006442.

811 Ludwig, K.R., 2003, Isoplot/Ex version 3.00, A Geochronological Toolkit for Microsoft Excel: Berkeley
812   Geochronology Center Special Publication 4.

813   Maiorani, A., Funiciello, R., Mattei, M., and Turi, B., 1992. Stable isotope geochemistry and structural
814   elements of the Sabina region (Central Apennines, Italy). Terra Nova, 4,484-488.

815   Malinverno, A., and Ryan, W.B.F., 1986. Extension in the Tyrrhenian Sea and shortening in the Apennines as
816   results of arc migration driven by sinking of the lithosphere. Tectonics, 5, 227–245,
817   doi:10.1029/TC005i002p00227.

818   Martini, I.P., and Sagri, M., 1993. Tectono-sedimentary characteristics of late Miocene–Quaternary
819   extensional basins of the Northern Apennines, Italy. Earth-Sci. Rev., 34, 197–233, doi: 10 .1016 /0012
820   -8252 (93)90034 -5.

821   Meckler, A. N., Ziegler, M., Millán, M. I., Breitenbach, S. F. M., Bernasconi, S. M., Millán, M. I., et al., 2014.
822   Long-term performance of the Kiel carbonate device with a new correction scheme for clumped isotope
823   measurements. Rapid Communications in Mass Spectrometry, 28(15), 1705–1715.
824   https://doi.org/10.1002/rcm.6949.

825   Miccadei, E., Barberi, R., and Cavinato, G.P., 1998. La geologia quaternaria della conca di Sulmona (Abruzzo,
826   Italia centrale). Geologica Romana, 34, 59-86.

827   Miccadei, E., Piacentini, T., Barberi, R., 2002. Uplift and local tectonic subsidence in the evolution of the
828   intramontane basins: the example of the Sulmona Basin (central Apennines, Italy). Studi Geologici
829   Camerti, Sp. Issue 2002, 119-133, http://dx.doi.org/10.15165/studgeocam-1368.

830   Miller, S.A., Collettini, C., Chiaraluce, L., Cocco, M., Barchi, M., Kaus, B.J.P., 2004. Aftershocks driven by
831   a high-pressure CO_2 source at depth. Nature 427, 724–727, http://dx.doi.org/10.1038/nature02251.

832   Minissale, A., 2004. Origin, transport and discharge of CO2 in central Italy. Earth-Sci. Rev., 66, 89-141.

833   Müller, I. A., Violay, M. E. S., Storck, J.-C., Fernandez, A., van Dijk, J., Madonna, C., & Bernasconi, S. M.,
834   2017. Clumped isotope fractionation during phosphoric acid digestion of carbonates at 70°C. Chemical
835   Geology, 449, 1–14. https://doi.org/10.1016/j.chemgeo.2016.11.030.

836   Özkul, M., Kele, S., Gökgöz, A., Shen, C.C., Jones, B., Baykara, M.O., Fórizs, I., Nemeth, T., Chang, Y.-W.,
837   and Alçiçek, M.C., 2013. Comparison of the Quaternary travertine sites in the Denizli extensional
838   basin based on their depositional and geochemical data. Sedimentary Geology, 294, 179–204, doi:
839   10.1016/j.sedgeo.2013.05.018.

840   Past Interglacials Working Group of PAGES, 2016. Interglacials of the last 800,000 years. Reviews of
841   Geophysics, 54, 162-219, doi:10.1002/2015RG000482.

842   Patacca, E., Scandone, P., Di Luzio, E., Cavinato, G.P., and Parotto, M., 2008. Structural architectures of the
843   Central Apennines: Interpretation of the CROP 11 seismic profile from the Adriatic coast to the
844   orographic divide. Tectonics, 27, TC3006, doi:10.1029/2005TC001917.

845   Petit, J.P., 1987. Criteria for the sense of movement on fault surfaces in brittle rocks. J. Struct. Geol. 9, 597–
846   608.

847   Pizzi, A., Di Domenica, A., Gallovič, F., Luzi, L., and Puglia, R., 2017. Fault segmentation as constraint to
848   the occurrence of the main shocks of the 2016 Central Italy seismic sequence. Tectonics, 36,
849   https://doi.org/10.1002/2017TC004652

850   Pizzi A., Di Domenica A., Di Federico P., Faure Walker J. P. & Roberts G., 2015. Geological investigation
851   along the Sulmona active normal fault (central Italy) and its effects on the seismic microzoning of the
852   area. Abstract Volume 6th International INQUA Meeting on Paleoseismology, Active Tectonics and
853   Archaeoseismology, 19-24 April 2015, Pescina, Fucino Basin, Italy.

854   Priewisch, A., Crossey, L.J., Karlstrom, K.E., Polyak, V.J., Asmerom, Y., Nereson, A., and Ricketts, J.W.,
855   2014. U-series geochronology of large-volume Quaternary travertine deposits of the southeastern

Colorado Plateau: Evaluating episodicity and tectonic and paleohydrologic controls. Geosphere, 10, 2, 401-423, doi:10.1130/GES00946.1.

Rihs, S., Condomines, M., and Poidevin, J.L., 2000. Long-term behaviour of continental hydrothermal systems: U-series study of hydrothermal carbonates from the French Massif Central (Allier Valley). Geochimica et Cosmochimica Acta, 64, 18, 3189–3199, doi:10.1016/S0016-7037(00)00412-9.

Roberts, G.P., and Michetti, A.M., 2004. Spatial and temporal variations in growth rates along active normal fault systems: an example from The Lazio–Abruzzo Apennines, central Italy. J. Struct. Geol., 26, 339-376.

Rovida, A., Locati, M., Camassi, R., Lolli, B., Gasperini, P., 2020. The Italian earthquake catalogue CPTI15. B. Earthq. Eng., 18(7), 2953-2984, https://doi.org/10.1007/s10518-020-00818-y

Rowland J.V. and Sibson R.H., 2004. Structural controls on hydrothermal flow in a segmented rift system, Taupo Volcanic Zone, New Zealand. Geofluids, 4, 259-283.

Schmid, T. W., & Bernasconi, S. M., 2010. An automated method for 'clumped-isotope' measurements on small carbonate samples. Rapid Communications in Mass Spectrometry, 24(14), 1955–1963. https://doi.org/10.1002/rcm.4598.

Sharp, Z., 2007. Principles of Stable Isotope Geochemistry. Pearson Prentice Hall. 344 pp.

Shen, C.-C., Cheng, H., Edwards, R.L., Moran, S.B., Edmonds, H.N., Hoff, J.A., and Thomas, R.B., 2003. Measurement of attogram quantities of ^{231}Pa in dissolved and particulate fractions of seawater by isotope dilution thermal ionization mass spectroscopy. Anal. Chem., 75, 1075–1079.

Shen, C.-C., Wu, C.-C., Cheng, H., Edwards, R.L., Hsieh, Y.-T., Gallet, S., Chang, C.-C., Li, T.-Y., Lam, D.D., Kano, A., Hori, M., and Spötl, C., 2012. High-precision and high-resolution carbonate ^{230}Th dating by MC-ICP-MS with SEM protocols. Geochim. Cosmochim. Acta, 99, 71–86.

Sibson, R.H., 1977. Fault rocks and fault mechanisms. J. Geol. Soc. London, 133, 191–213.

Sibson, R.H. (1992), Implications of fault-valve behavior for rupture nucleation and recurrence, Tectonophysics 18, 1031–1042.

Sibson, R.H., 2014. Earthquake rupturing in fluid-overpressured crust: how common? Pure Appl. Geophys. 171, 2867–2885. http://dx.doi.org/10.1007/s00024-014-0838-3.

Sibson, R.H. and Rowland, J.V., 2003. Stress, fluid pressure and structural permeability in seismogenic crust, North Island, New Zealand. Geophys. J. Int., 154, 584-594.

Smeraglia, L., Bernasconi, S.M., Berra, F., Billi, A., Boschi, C., Caracausi, A., Carminati, E., Castorina, F., Doglioni, C., Italiano, F., Rizzo, A.L., Uysal, T., and Zhao, J.X., 2018. Crustal-scale fluid circulation and co-seismic shallow comb-veining along the longest normal fault of the central Apennines, Italy. Earth Planet. Sc. Lett. 498, 152–168, https://doi.org/10.1016/j.epsl.2018.06.013.

Smeraglia, L., Berra, F., Billi, A., Boschi, C., Carminati, E., Doglioni, C., 2016. Origin and role of fluids involved in the seismic cycle of extensional faults in carbonate rocks. Earth Planet. Sc. Lett. 450, 292–305, http://dx.doi.org/10.1016/j.epsl.2016.06.042.

Smith, S.A.F., Billi, A., Di Toro, G., Spiess, R., 2011. Principal slip zones in limestone: microstructural characterization and implications for the seismic cycle (Tre Monti fault, Central Apennines, Italy). Pure Appl. Geophys. 168, 2365–2393.

Sturchio, N.C., Pierce, K.L., Murrell, M.T., and Sorey, M.L., 1994. Uranium-series ages of travertines and timing of the last glaciation in the northern Yellowstone area, Wyoming–Montana. Quaternary Research, 41, 265–277, doi: 10 .1006 /qres .1994 .1030.

898 Tesei, T., Collettini, C., Viti, C., Barchi, M.R., 2013. Fault architecture and deformation mechanisms in
899   exhumed analogues of seismogenic carbonate-bearing thrusts. J. Struct. Geol. 55, 167-181,
900   http://dx.doi.org/10.1016/j.jsg.2013.07.007.

901 Tzedakis, P.C., Andrieu, V., de Beaulieu, J.-L., Birks, H.J.B., Crowhurst, S., Follieri, M., Hooghiemstra, H.,
902   Magri, D., Reille, M., Sadori, L., Shackleton, N.J., and Wijmstra, T.A., 2001. Establishing a terrestrial
903   chronological framework as a basis for biostratigraphical comparisons. Quaternary Science Reviews,
904   20, 1583-1592, doi:10.1016/S0277-3791(01)00025-7.

905 Uysal, I.T., Feng, Y., Zhao, J.X., Isik, V., Nuriel, P., and Golding, S.D., 2009. Hydrothermal CO_2 degassing
906   in seismically active zones during the late Quaternary. Chemical Geology, 265, 442–454, doi:
907   10.1016/j.chemgeo.2009.05.011.

908 Vezzani, L., Festa, A., and Ghisetti, F.C., 2010. Geology and tectonic evolution of the central-southern
909   Apennines, Italy. Geol. Soc. Am. Sp. Paper, 469, 58 p., doi: 10.1130/2010.2469.

910 Vignaroli, G., Berardi, G., Billi, A., Kele, S., Rossetti, F., Soligo, M., Bernasconi, S.M., 2016. Tectonics,
911   hydrothermalism, and paleoclimate recorded by Quaternary travertines and their spatio-temporal
912   distribution in the Albegna basin, central Italy: insights on Tyrrhenian margin neotectonics. Lithosphere
913   8, 335–358.

914 Vignaroli, G., Mancini, M., Brilli, M., Bucci, F., Cardinali, M., Giustini, F., Voltaggio, M., Yu, T.-L., Shen,
915   C.-C., 2020a. Spatial-temporal evolution of extensional faulting and fluid circulation in the Amatrice
916   Basin (central Apennines, Italy) during the Pleistocene. Front. Earth Sci. 8:130, doi:
917   10.3389/feart.2020.00130.

918 Vignaroli, G., Viola, G., Diamanti, R., Zuccari, C., Garofalo, P.S., Bonini, S., Selli, L., 2020b. Multistage
919   strain localisation and fluid-assisted cataclasis in carbonate rocks during the seismic cycle: insights from
920   the Belluno Thrust (eastern Southern Alps, Italy). Journal of Structural Geology,
921   https://doi.org/10.1016/j.jsg.2020.104216.

922 Wang, X., Auler, A.S., Edwards, R.L., Cheng, H., Cristalli, P.S., Smart, P.L., Richards, D.A., Shen, C.C.,
923   2004. Wet periods in northeastern Brazil over the past 210 kyr linked to distant climate anomalies.
924   Nature, 432, 740-743.

925 Wedepohl, K., 1995, The composition of the continental crust: Geochim. Cosmochim. Acta, v. 59, p. 1217-
926   1239.

927 Williams, R.T., Goodwin, L.B., Mozley, P.S., Beard, B.L., Johnson, C.M., 2015. Tectonic controls on fault
928   zone flow pathways in the Rio Grande rift, New Mexico, USA. Geology 43, 723–726.
929   http://dx.doi.org/10.1130/G36799.1.

930 Zachos, J., Pagani, M., Sloan L., Thomas, E., Billups, K., 2001. Trends, Rhythms, and Aberrations in Global
931   Climate 65 Ma to Present. Science, 292, 686-693, doi: 10.1126/science.1059412.

932

933

934

935

936

Captions to Figures

Figure 1. Structural scenario of the fault-valve mechanism framed within the seismic cycle. The creation of fault permeability is here correlated to the tectonics, mineralisation, and fluid pressure cycling. EQ: earthquake.

Figure 2. a) Schematic tectonic framework of the Apennines within the western Mediterranean region; b) geological setting of the central Apennines, where the distribution of both the main thrust fronts and the active normal faults is reported (modified and readapted after Cosentino et al., 2010). The map also shows the localisation of both the main recent earthquakes (including their focal mechanisms) and the historical earthquakes in the area surrounding the Monte Morrone. The seismic data are after Amato et al. (1998), Chiarabba et al. (2009), Chiaraluce et al. (2017), and the Parametric Catalogue of Italian Earthquakes (CPTI15 available at https://emidius.mi.ingv.it/CPTI15-DBMI15/index_en.htm). The location of two dated faults (Val Roveto Fault: Smeraglia et al., 2018; Amatrice Fault System: Vignaroli et al., 2020a) and dated Quaternary travertines (Semproniano-Saturnia travertines: Berardi et al., 2016; Vignaroli et al., 2016; Radicofani and Val di Chiana travertines; Brogi et al., 2010; 2012; 2017) is also shown; c) geological setting of the Monte Morrone area showing the orientation and distribution of the western (WFS) and eastern (EFS) strands of the Monte Morrone Fault System (modified after Pizzi et al., 2015); d) schematic cross section illustrating the main stratigraphic/structural setting of the Monte Morrone-Sulmona Basin system (modified after Miccadei et al., 2002). The Monte Morrone Fault System cuts through the Meso-Cenozoic carbonate bedrock and accommodates more than 400 m-thick Quaternary continental deposits filling the Sulmona Basin; e) Google Earth © view of the study area around the Roccacasale village, showing the localisation of structural sites along the western strand of the Monte Morrone Fault System. AFS: Amatrice fault System; SeSa: Semproniano-Saturnia travertines; VRF: Val Roveto Fault.

Figure 3. Structural features of the western strand of the Monte Morrone Fault System observed at the studied outcrops. a) Panoramic view of the main fault surface exposed southeast to the Roccacasale village (structural stop M3.1 in Fig. 2e). In the insert: stereographic projection (Schmidt net, lower hemisphere) of the measured main slip surfaces; b) dip-slip slickenlines (rock abrasion) exposed on the fault surface; c) metre-thick damage zone, produced at the expense of Meso-Cenozoic carbonate bedrock, occurring at the footwall of the main slip surface (structural stop M3.2 in Fig. 2e; compare with Fig. 4b of Ferraro et al., 2018); d) outcrop view of the fault damage zone exposed northwest to the Roccacasale village (structural stop M4.1 in Fig. 2e) where the carbonate mineralisations were collected; e) the damage zone is characterised by lenses of foliated or massive cataclasites produced at the expense of the Mesozoic limestone.

Figure 4. Mesoscopic properties of the WFS at the structural stop M4.1 (see Fig. 2e and Table 1 for location). a) Damage zone around the main slip surface that is, in turn, cross cut by a set of high-angle normal faults; b) detail of the crosscutting relationships between the main slip surface and the high-angle normal faults, the latter producing decimetre-to-half metre offset; c) high-angle normal fault crosscutting the main slip surface, the latter decorated by cm-thick carbonate mineralisation; d) detail of two separated cm-thick carbonate mineralisation occurring atop the main slip surface; e) detail of the main slip surface intervening between a massive cataclasite (at the footwall) and a dm-to-cm-thick mineralisation (at the hanging wall); f) enlargement of the previous image (the broken mineralisation is here exposed) showing the internal fabric of the carbonate mineralisation; g) and h) structural and petrographical details of high-angle faults, where thin (a few mm) patina of carbonate mineralisation occurs on the slickensided surface. Samples used for microstructural investigation and geochemical/geochronological purposes are indicated by red labels.

Figure 5. Example of rock slab (sample M4G; Table 1) used for defining the main observed structural fabrics. (a) Polished rock slab of sample M4G with the indication of micro-drilling sites for geochemical and geochronological purposes. U-Th ages and temperatures deriving from clumped isotopes analysis are also indicated; (b) scanned thin section of sample M4G showing, from bottom to top, the cataclasite, the main slip surface, the sedimentary breccias (probably filling voids of karst origin) and three main mineralisations

986 characterised by a layering of thin laminae and sparitic veins; (c) line drawing of the main features observed
987 in the scanned thin section of sample M4G; (d) and (e) BSE images (see Fig. 5b for location) showing the
988 main slip surface, sub-rounded small clasts in the ultracataclasite, sub-angular clasts and clasts with
989 polygonal fractures; (f) enlargement of Fig 5e.

990 **Figure 6.** Microscale properties of the collected samples. a) Petrographic image (crossed polarised light) of
991 massive cataclasite consisting of a fine- to very fine-grained matrix embedding a few large clasts (up to 1.5
992 mm in width); (b) back-scattered electron (BSE) image showing the occurrence of polygonal fractures within
993 the cataclasite; c) BSE image showing the occurrence of a slip surface that sharply truncate the carbonate
994 clasts; d) petrographic image (plane polarised light) and e) cathodoluminescence image showing traces of
995 permeating fluid (bright colour in cathodoluminescence) within the fine-grained cataclasite matrix; f)
996 petrographic image (plane polarised light) and g) cathodoluminescence image showing layered (and partly
997 folded) carbonate mineralisation atop a very fine-grained cataclasite. Note the general upward-convex fan-
998 shaped crystals grown during incremental layering. Cathodoluminescence imaging reveals that calcite
999 making the mineralisation is characterised by a dark violet colour, darker than the colour of the adjacent
1000 cataclasite; h) petrographic image (plane polarised light) and i) BSE image showing fractured mineralisation
1001 embedded within the fine-grained cataclasite; j) petrographic image (crossed polarised light) showing
1002 polyphasic growth of mineralisation embedding lenses of protocataclasite. Note the different style of
1003 growing (including bedding-parallel layers, undulate layers, elongated crystals); k) upward-convex fan-
1004 shaped crystals grown and downward-convex fan-shaped crystals grown in mineralisations separated by a
1005 thin layer of cataclasite.

1006 **Figure 7.** Line drawing of the studied outcrop (Fig. 3d) with indication of the selected mineralisation
1007 samples for U-Th ages. The insets indicate the mineralisation slabs, as well as the selected portion for U-Th
1008 analysis and the obtained results.

1009 **Figure 8.** Combined plot of $\delta^{13}C$ (‰V-PDB) and $\delta^{18}O$ (‰V-PDB) isotope values derived from the collected
1010 samples. V-PDB: Vienna Peedee Belemnite standard.

1011 **Figure 9.** a) simplified structural architecture of the MMFS as deduced from observation at the studied
1012 outcrops; b) schematic scenario of fault permeability development during the progressive exhumation of the
1013 of the fault core-damage zone formed at depth (at t_n) and reactivation of slip surfaces at shallower crustal
1014 conditions (at t_{n+nx}); c) structural relationships between the analysed carbonate mineralisations and the fault
1015 domains as documented by previous work on the same fault strands (Ferraro et al., 2018; Coppola et al.,
1016 2021); d) two-stage structural evolution for the MMFS according to fault cross-cutting relationships, pattern
1017 of fluid circulation during faulting as deduced from the isotopic analysis, and absolute ages provided by U-
1018 Th dating on carbonate mineralisations; e) proposed scenario of cyclical fault-fluid interactions in the MMFS
1019 within a recurrence time of 10-15 ka between coseismic events as deduced from this study. fc: fault core; dz:
1020 damage zone. EFS and WFS are the eastern and western strands of the Monte Morrone Fault System,
1021 respectively.

1022 **Figure 10.** Comparison between U-Th ages of fault-related mineralisations from the MMFS (this study), the
1023 Amatrice fault System (AFS; Vignaroli et al., 2020a), the Val Roveto Fault (Smeraglia et al., 2018) and
1024 $CaCO_3$ samples (bedded and banded travertines, calcite-filled veins) from the northern part of the central
1025 Apennines (Sem-Sat: Semproniano-Saturnia travertines: Berardi et al., 2016; Vignaroli et al., 2016; Ra-VdC:
1026 travertines from the Radicofani and Val di Chiana basins: Brogi et al., 2010; 2012; 2017; see location in Fig.
1027 2b). Major paleoclimate indicators are represented by the deep-sea oxygen isotope trend (Zachos et al.,
1028 2001), the pollen data set from Valle di Castiglione (Tzedakis et al., 2001), and the atmospheric CO_2
1029 degassing (Past Interglacial Working Group of PAGES, 2016). Glacial-interglacial periods are redrawn and
1030 modified after Priewisch et al. (2014). Valle di Castiglione is located in central Italy (see location in Fig. 2b)
1031 only ~100 km west to the MMFS. MIS: Marine Isotope Stages. AP: arboreal pollen; NAP: non-arboreal
1032 pollen. Eccentricity/precession are redrawn and modified after Past Interglacial Working Group of PAGES
1033 (2016).

Table 1. Summary of observed structures and collected samples during the structural survey along the western strand of the Monte Morrone Fault System (see Fig. 2e).

Table 2. U-Th ages of the carbonate mineralisations from the Monte Morrone Fault System collected at the studied outcrop near Roccacasale village (site M4.1; long.: 13.883°; lat.: 42.125°). Sample indicated with * was analysed through MC-ICP-MS at the HISPEC of the National Taiwan University (errors quoted as 2σ), whereas sample indicated with ** was analysed through α spectrometry done at the at the Laboratory of Environmental and Isotopic Geochemistry (Department of Sciences, Roma Tre University, Italy) (errors quoted as 1σ).

Table A1. Stable oxygen and carbon isotope composition of the selected samples from the Monte Morrone Fault System collected at the studied outcrop near Roccacasale village (long.: 13.883°; lat.: 42.125°). Isotope compositions are expressed in ‰ against Vienna Pee Dee Belemnite standard (VPDB).

Table A2. Clumped isotopes analyses on the selected samples from the Monte Morrone Fault System.

Figure SM1. Polished rock slabs of the analysed samples (sample M4G is reported in Fig. 5; Tables 1 and 2) with the indication of micro-drilling sites for geochemical (stable isotopes in black and clumped isotopes in red) and geochronological analysis (red-white circles). U-Th ages and temperatures deriving from clumped isotopes analysis are also indicated.

Figure SM2. Polished slab, high-resolution scanned thin section, detailed petrographic and back-scattered electron (BSE) images showing the main observed structural fabrics of sample M4HW. a) Oriented polished rock slab showing the contact between the slip surface (here developed at the top of the carbonate mineralisation) and the hanging wall of the massive cataclasite; b) high-resolution scanned thin section of sample M4HW showing the carbonate mineralisations (at the bottom) and cataclasite (at the top); c) petrographic image (crossed polarised light) showing brecciated mineralisations partially embedded within the fine-grained cataclasite. Secondary cement made by calcite crystals occurs within the reworked carbonate mineralisations; d) petrographic image (plane polarized light) showing sigmoidal foliation within the carbonate mineralisations embedded in two minor slip surfaces; e) petrographic image (plane polarised light) showing fractured and brecciated carbonate mineralisations with several minor slip surfaces and embedding pockets of protocataclasites; f) BSE image showing the main slip surface at the top of the carbonate mineralisations and the fractured mineralisations partially embedded in the cataclasite. Note the two extensional fractures developed along the main slip surface; g) BSE image showing structures high angle to vertical slip surface, generally with undulating boundaries and characterised by tight cataclasite and calcite vein.

Figure SM3. Petrographic images showing the microscale properties of M4H2 sample at different scale of observation. (a) Petrographic photomosaic (plane polarised light) of the lower part of M4H2 thin section showing (at the bottom) multiple generation of mineralisations (formed both by laminae and veins) and breccia (at the top). The upper edge of the mineralisation is characterized by a thin layer of ultracataclasite. At least one slip surface is observed within the mineralisation. (b) Petrographic image (plane polarised light) showing within the breccia clasts of former mineralisations mixed with other carbonate fragments deriving from previous cataclasite and calcite cement. (c-d) Petrographic images (plane and crossed polarised light, respectively) showing a series of bands of cataclasite and ultracataclasite within the mineralisation. (e) Petrographic image (plane polarised light) showing the upper edge of the mineralisation covered by a thin layer of ultracataclasite. (f-g) Petrographic images (plane and crossed polarised light, respectively) showing a series of bands parallel to the slip surface and formed by cataclasites alternating with highly fractured mineralisations. The upper portion of the mineralisation is flattened and truncated along the slip surface and some fragments of the mineralisation are partially embedded within the thin layer of ultracataclasite. (h-i) Petrographic images (plane and crossed polarised light, respectively) showing in detail a series of bands parallel to the slip surface and formed by cataclasites alternating with highly fractured mineralisations. Interposed between two bands of cataclasite, a thin level of mineralisation is highly fractured, and some carbonate clasts are partially dispersed in the cataclasite. (l-m) Petrographic images (plane and crossed

1082 polarised light, respectively) showing a highly fractured portion of the mineralisation with a shape miming a
1083 sigmoidal foliation. (n-o) Petrographic images (plane and crossed polarised light, respectively) showing in
1084 detail the upper portion of the mineralisation. A thin layer of ultracataclasite, with some synthetic shear zone,
1085 covers the edge of the mineralisation.

1086

1087

Table 1

TABLE 1. Summary of observed structures and collected samples during the structural survey along the western strand of the Monte Morrone Fault System (see Fig. 2e).

Structural stop	Lat.	Long.	Structural fabric	Sample for geochronology (Table 2)	Sample for isotope data (Table A1)
M1	42.124°	13.888°	• Damage zone (synthetic faults and extensional or hybrid fractures)		
M3.1	42.121°	13.893°	• Fault core (main slip surface and cataclasite) • High-angle normal faults cutting the main slip surface		
M3.2	42.121°	13.894°	• Fault core (main slip surface and cataclasite)		
M4.1	42.125°	13.883°	• Fault core (main slip surface, cataclasite, fault breccias and veins made by calcite precipitation) • Damage zone (synthetic faults and extensional or hybrid fractures) • High-angle normal faults cutting the main slip surface	M4G/1, M4G/2, M4G/3, M4H, M4H2, M4HW, M4F1, M4i, M4e	M4G/1, M4G/2, M4G/3, M4H, M4H2, M4HW, M4F1, M4i, M4e
M4.2	42.127°	13.882°	• Fault core (main slip surface and cataclasite) • High-angle normal faults cutting the main slip surface		
M4.3	42.128°	13.881°	• Fault core (main slip surface and cataclasite) • High-angle normal faults cutting the main slip surface		
M4.4	42.129°	13.879°	• Damage zone (synthetic faults and extensional or hybrid fractures)		

Table 2

Table 2. U-Th ages of the carbonate mineralisations from the Monte Morrone Fault System collected at the studied outcrop near Roccacasale village (site M4.1; lat.: 42.125° N; long.: 13.883° E). Sample indicated with * was analysed through MC-ICP-MS at the HISPEC of the National Taiwan University (errors quoted as 2σ), whereas sample indicated with ** was analysed through α spectrometry done at the at the Laboratory of Environmental and Isotopic Geochemistry (Department of Sciences, Roma Tre University, Italy) (errors quoted as 1σ).

Sample ID	Weight g	^{238}U Ppb (a)	^{232}Th ppb	$\delta^{234}U$ measured (a)	$[^{230}Th/^{238}U]$ activity (c)	$^{230}Th/^{232}Th$ atomic (x 10^{-6})	Age (ka ago) uncorrected	Age (ka ago) corrected (c,d)	$\delta^{234}U_{initial}$ corrected (b)
M4G/1*	0.2311	154.95 ± 0.16	0.1216 ± 0.0020	21.6 ± 1.4	0.9030 ± 0.0018	18969 ± 315	230.3 ± 2.0	230.3 ± 2.0	41.5 ± 2.6
M4G/2*	0.21021	244.15 ± 0.28	0.4809 ± 0.0023	6.0 ± 1.4	0.9027 ± 0.0018	7556 ± 38	246.6 ± 2.5	246.6 ± 2.5	12.1 ± 2.8
M4G/3*	0.19458	198.01 ± 0.27	2.5449 ± 0.0055	7.7 ± 1.6	0.9149 ± 0.0033	1173.6 ± 4.6	257.8 ± 4.3	257.4 ± 4.3	15.8 ± 3.3
M4H*	0.20549	419.68 ± 0.51	10.833 ± 0.033	9.8 ± 1.5	0.9264 ± 0.0046	591.7 ± 3.4	268.6 ± 6.2	267.9 ± 6.1	20.9 ± 3.2
M4H2*	0.22826	429.58 ± 0.55	11.059 ± 0.036	17.6 ± 1.8	0.8848 ± 0.0043	566.7 ± 3.3	219.0 ± 3.7	218.3 ± 3.7	32.6 ± 3.3
M4HW*	0.21036	255.88 ± 0.38	15.445 ± 0.067	24.5 ± 1.8	0.8902 ± 0.0086	243.2 ± 2.5	217.3 ± 6.7	215.8 ± 6.7	45.1 ± 3.3
M4F1*	0.20277	323.87 ± 0.38	0.2808 ± 0.0023	8.9 ± 1.7	0.8703 ± 0.0020	16552 ± 141	214.9 ± 2.1	214.9 ± 2.1	16.4 ± 3.2
M4i*	0.2008	138.40 ± 0.15	2.0115 ± 0.0033	23.6 ± 1.3	0.8483 ± 0.0039	962.4 ± 4.6	189.7 ± 2.5	189.4 ± 2.5	40.3 ± 2.3

Sample ID	U (ppm)	$^{230}Th/^{232}Th$	$^{234}U/^{238}U$	$^{230}Th/^{234}U$	$(^{234}U/^{238}U)$ initial	Age (ka)
M4e**	0.137 ± 0.005	83.105±10.401	1.030±0.037	0.809±0.036	1.050±0.061	178 +39/-30

(a) $[^{238}U] = [^{235}U]$ x 137.818 (±0.65‰) (Hiess et al., 2012); $\delta^{234}U = ([^{234}U/^{238}U]_{activity} - 1)$ x 1000.

(b) $\delta^{234}U_{initial}$ corrected was calculated based on ^{230}Th age (T), i.e., $\delta^{234}U_{initial} = \delta^{234}U_{measured} X e^{\lambda 234*T}$, and T is corrected age.

(c) $[^{230}Th/^{238}U]_{activity} = 1 - e^{-\lambda_{230}T} + (\delta^{234}U_{measured}/1000)[\lambda_{230}/(\lambda_{230} - \lambda_{234})](1 - e^{-(\lambda_{230} - \lambda_{234})T})$, where T is the age. Decay constants are 9.1705 x 10^{-6} yr^{-1} for ^{230}Th, 2.8221 x 10^{-6} yr^{-1} for ^{234}U (Cheng et al., 2013), and 1.55125 x 10^{-10} yr^{-1} for ^{238}U (Jaffey et al., 1971).

(d) Age corrections, relative to chemistry date on March 19th, 2019, were calculated using an estimated atomic $^{230}Th/^{232}Th$ ratio of 4 (± 2) x 10^{-6}.

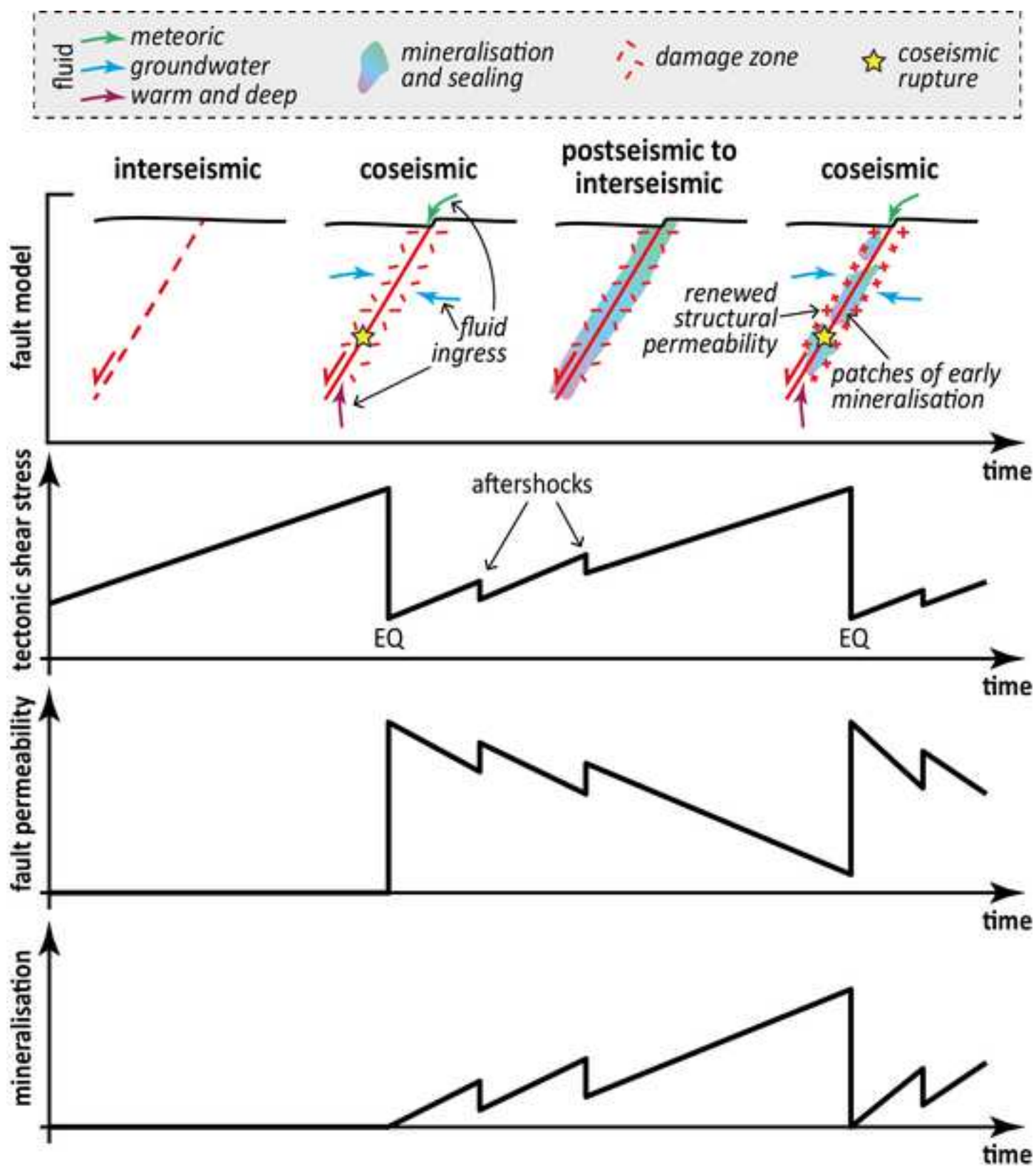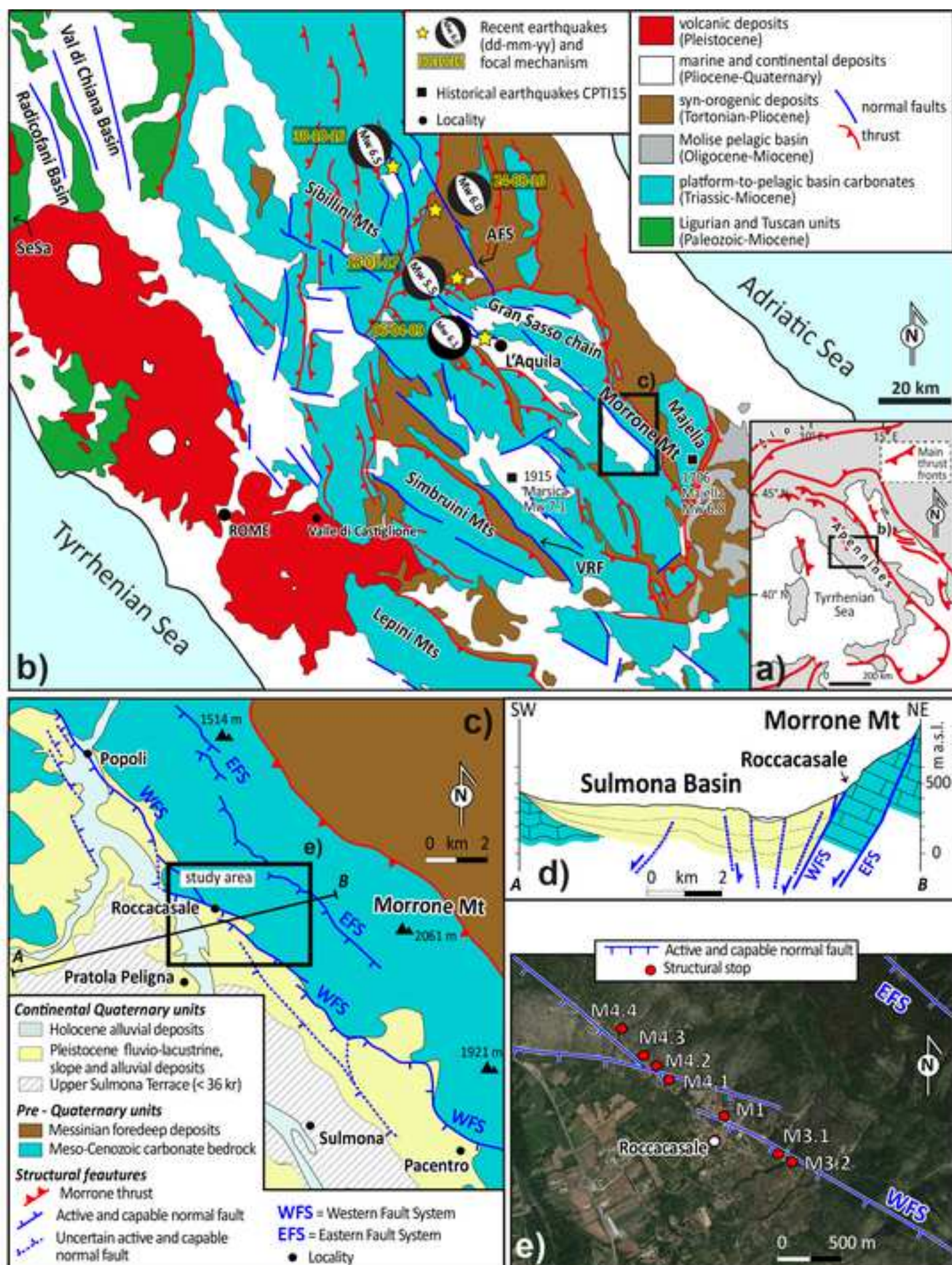Those are the values for a material at secular equilibrium, with the crustal $^{232}Th/^{238}U$ value of 3.8. The errors are arbitrarily assumed to be 50%.
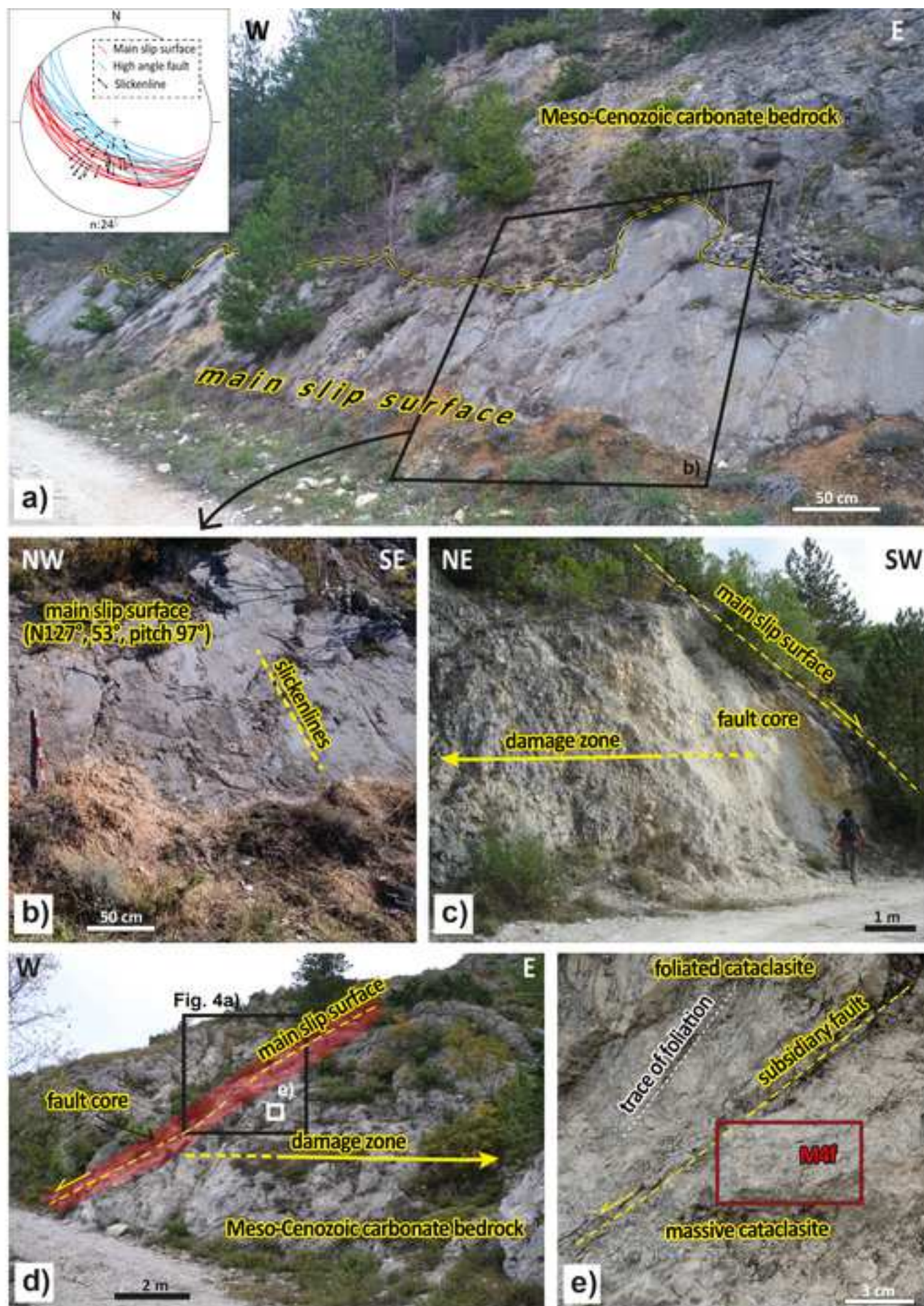
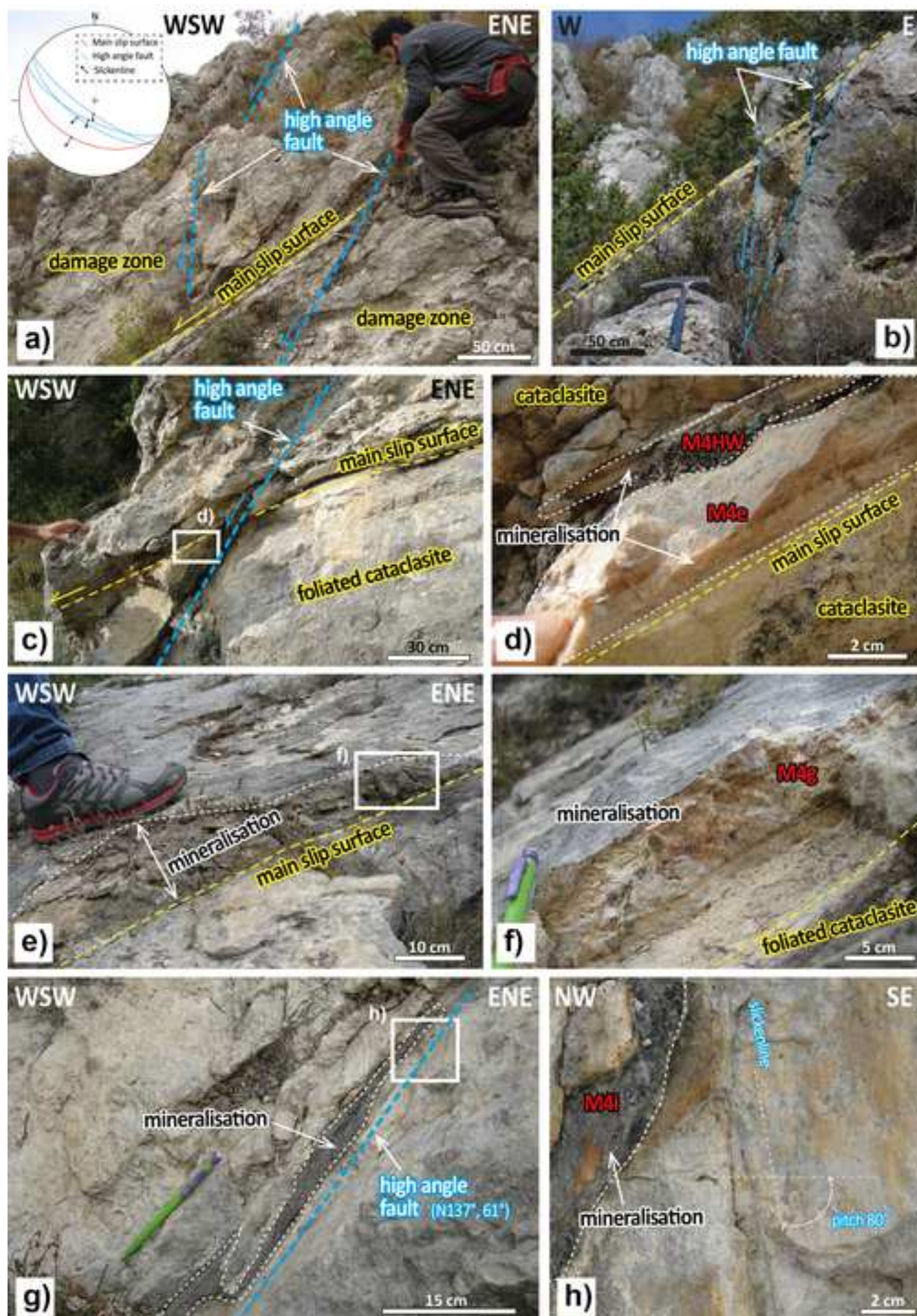Figure 1

Figure 2

Figure 3

Figure 4

Figure 5

a)

SW ←

230.3 ±2.0

M4G_1e 23 °C

M4G_2a 26 °C

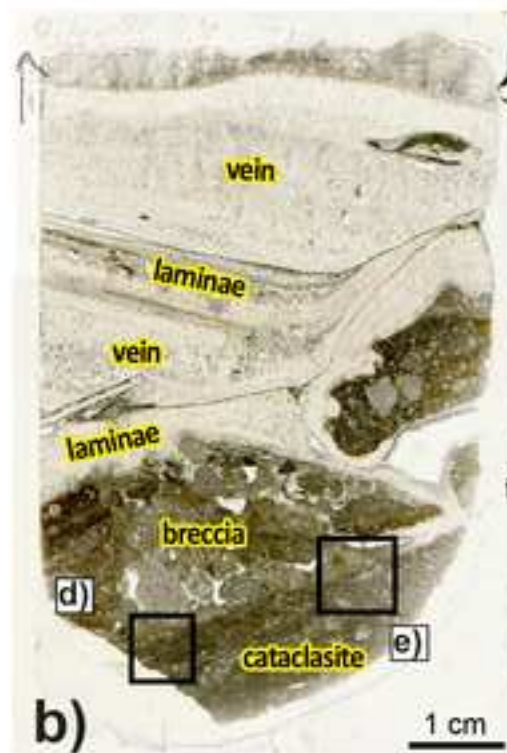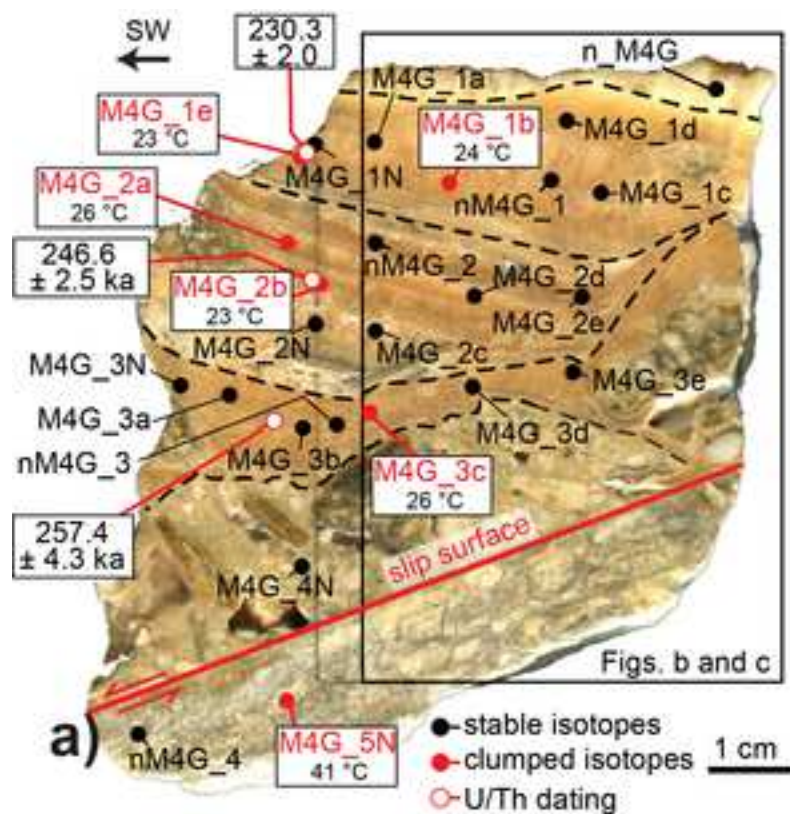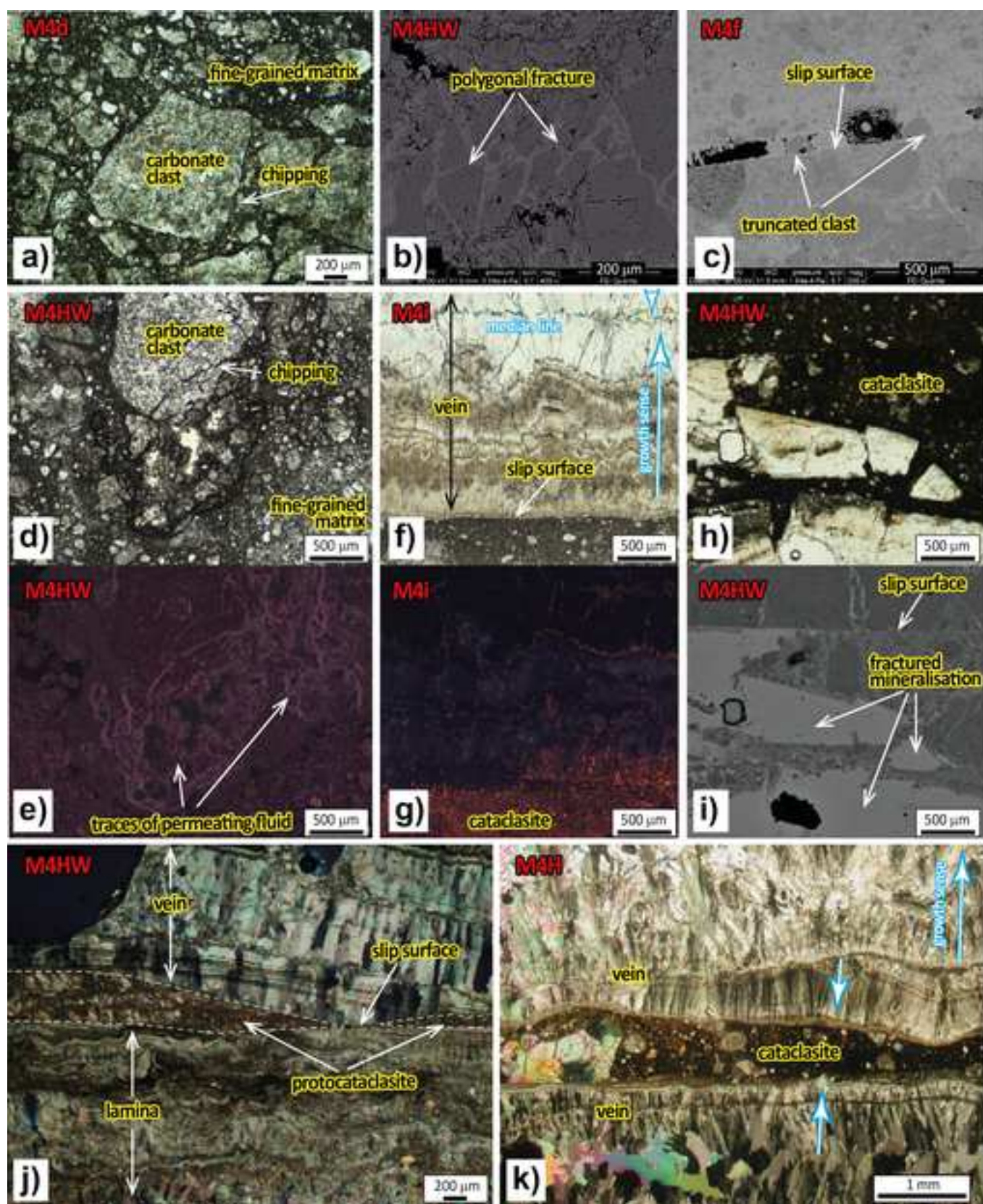246.6 ± 2.5 ka

M4G_2b 23 °C

257.4 ± 4.3 ka

M4G_3c 26 °C

M4G_5N 41 °C

n_M4G

M4G_1a

M4G_1b 24 °C

M4G_1d

M4G_1N

nM4G_1

M4G_1c

nM4G_2

M4G_2d

M4G_2e

M4G_2N

M4G_2c

M4G_3N

M4G_3e

M4G_3a

M4G_3d

nM4G_3

M4G_3b

slip surface

M4G_4N

nM4G_4

Figs. b and c

● stable isotopes
● clumped isotopes
○ U/Th dating

1 cm

b)

vein

laminae

vein

laminae

breccia

cataclasite

d)

e)

1 cm

c)

mineralisation 1

mineralisation 2

mineralisation 3

protolith clast

cataclastic clast

fine-grained matrix

calcite rim

cataclastic clast

cataclastic clast

protolith clast

1 cm

d)

slip surface

ultracataclasite

sigmoidal foliation

e)

uncracked clast

slip surface

f)

cracked clasts

f)

uncracked clast

slip surface

ultracataclasite

cracked clasts

Figure 6

Figure 7

M4H — cataclasite — 1 cm — mineralisation — 267.9 ± 6.1 ka

M4h2 — 1 cm — 218.3 ± 3.7 ka — mineralisation — cataclasite

M4i — mineralisation — 189.4 ± 2.5 ka — 1 cm

high angle fault

main slip surface

M4h2
M4H
M4i
M4G
M4f1
M4HW
M4e

M4HW — cataclasite — 1 cm — mineralisation — 215.8 ± 6.7 ka

2 m

178 +39/-30 ka — mineralisation — cataclasite — M4e — 1 cm

M4f1 — mineralisation — 214.9 ± 2.1 ka

M4G — mineralisation — 230.3 ± 2.0 ka — 246.6 ± 2.5 ka — 257.4 ± 4.3 ka — cataclasite — 5 cm
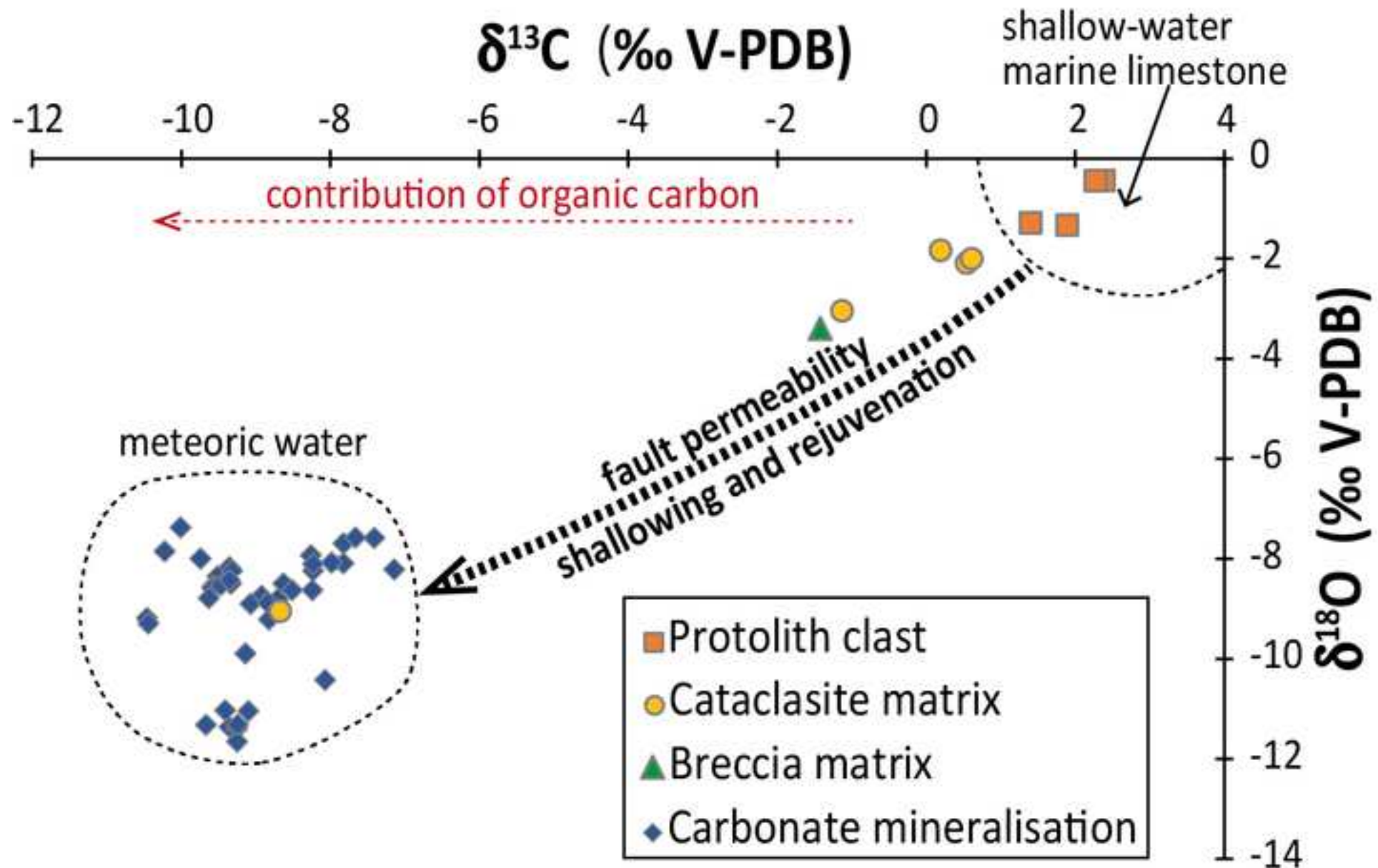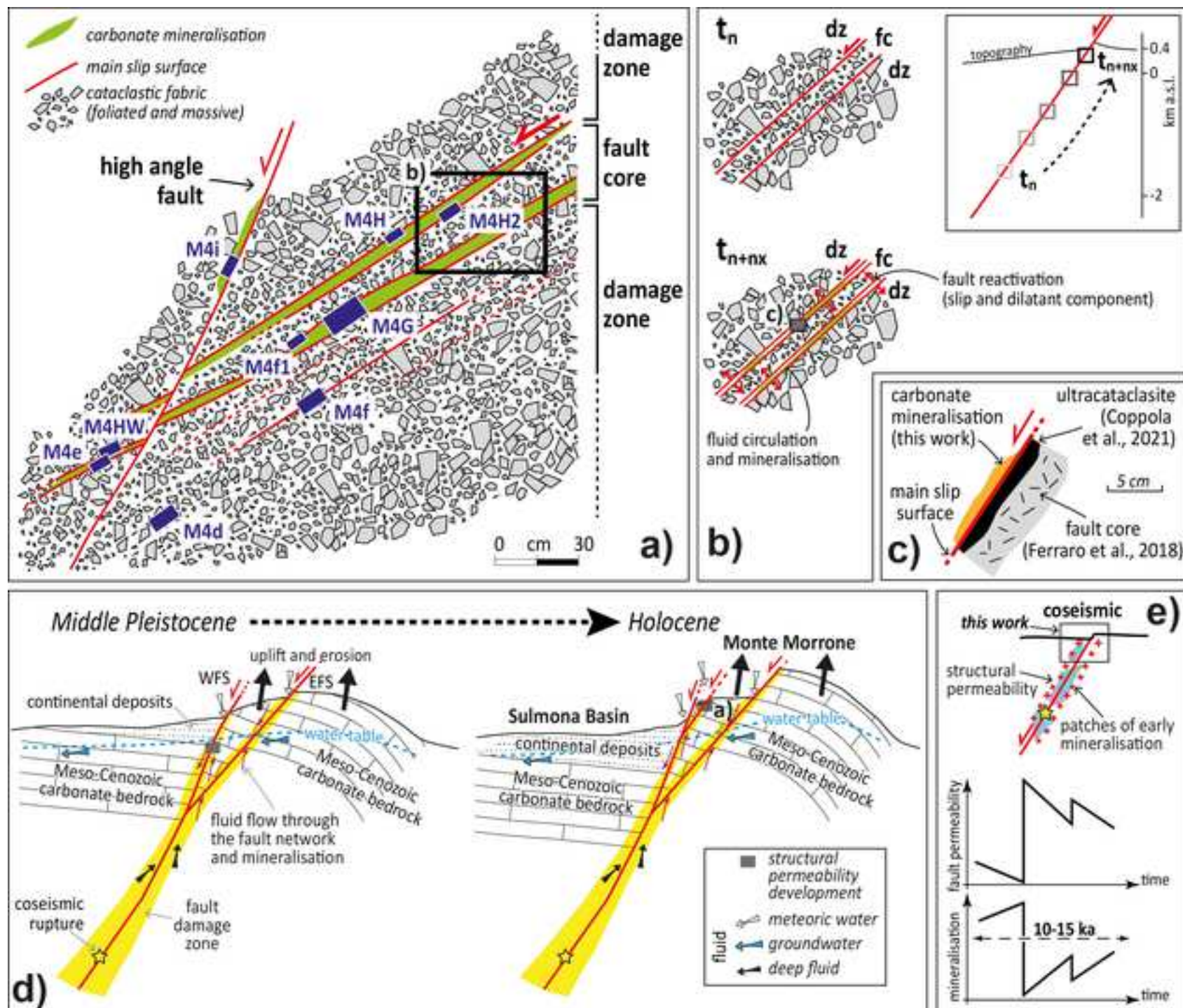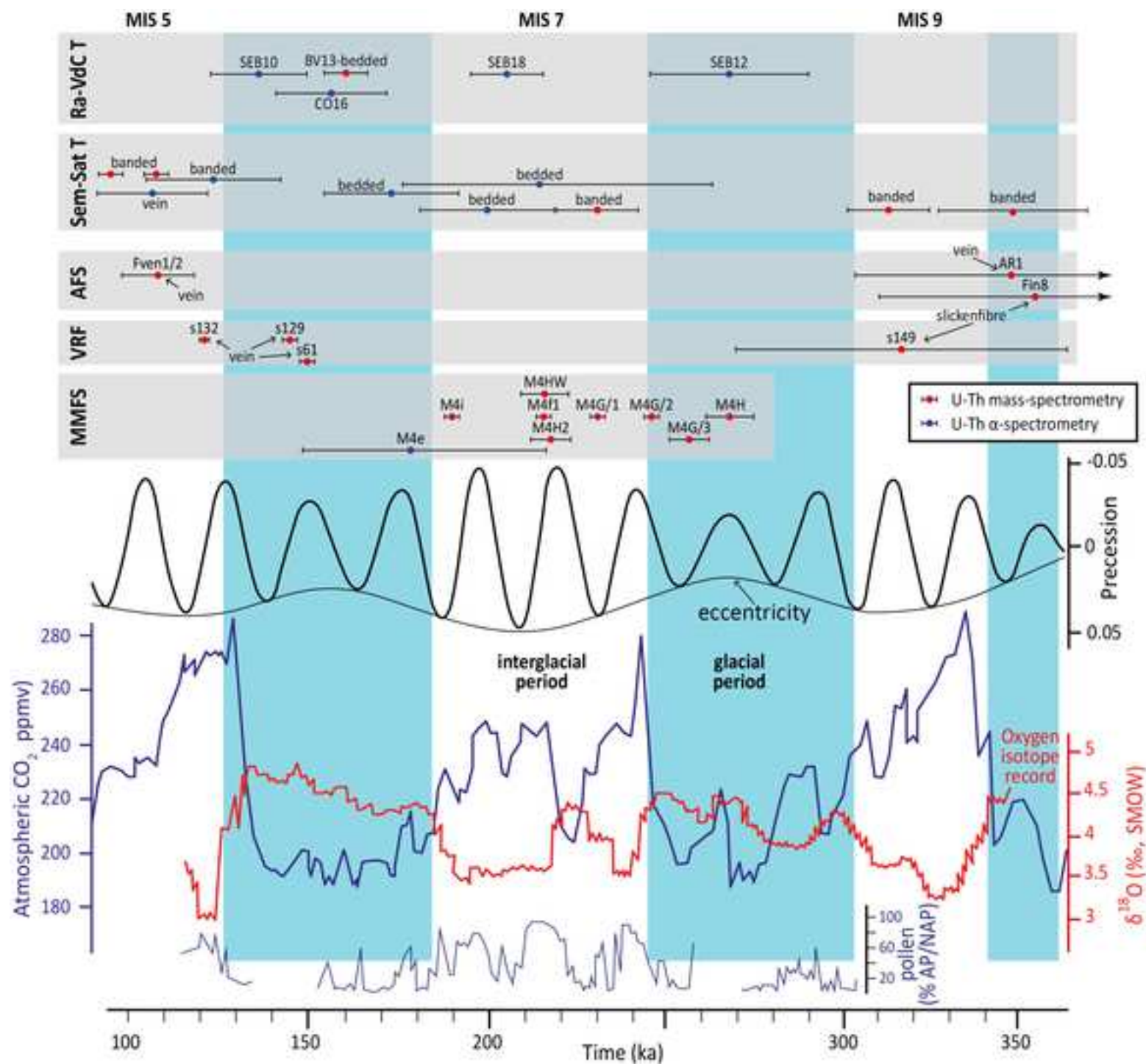
Figure 8

Figure 9

Figure 10

Credit author statement

Gianluca Vignaroli: Methodology, Investigation, Data curation, Visualisation, Writing - original draft, review & editing

Federico Rossetti: Validation, Investigation, Resources, Writing - review & editing, Supervision

Lorenzo Petracchini: Investigation, Data curation, Visualisation, Writing - review & editing

Valentina Argante: Investigation, Data curation, Visualisation, Writing - original draft

Stefano M. Bernasconi: Formal analysis, Investigation, Resources, Writing - review & editing

Mauro Brilli: Validation, Formal analysis, Investigation, Writing - review & editing

Francesca Giustini: Validation, Formal analysis, Investigation, Writing - review & editing

Tsai-Luen Yu: Validation, Formal analysis, Investigation, Writing - review & editing

Chuan-Chou Shen: Validation, Formal analysis, Investigation, Resources, Writing - review & editing

Michele Soligo: Validation, Formal analysis, Investigation, Resources